Supplementary Information (SI) for Chemical Science.

Supplementary Information

2D Spatial Structure Favored Tandem Catalysis Boosted Methane Direct Transformation to Methanol over Cu-FER

*Ning Liu, Tingting Zhang, Chengna Dai, Ruinian Xu, Ganqiang Yu, Ning Wang, Biaohua Chen**

College of Environmental and Science Engineering, Beijing University of Technology, Beijing,

100124, China

*Correspondence to: chenbh@bjut.edu.cn

Table of Content

Activity measurement method

The N_2O-DMTM activity measurement was carried out in a fixed-bed quartz reactor (Outer Diameter: 11 mm, Inner Diameter: 8 mm, Length: 485 mm). The products were analyzed online using a SHIMADZU GC-2014 gas chromatograph equipped with a thermal conductivity detector (TCD) and a flame ionization detector (FID). The automatic injection system consisted of two inlet valves (ten-way and six-way) and four packed columns. Separation of CH_4, N_2O, CO_2, N_2, and O_2 was achieved using a Porapak Q (PQ) column (1.0 m × 3.2 mm × 2.1 mm), connected with a Hayesep D column (2.0 m × 3.2 mm × 2.1 mm) and a Molecular Sieve-13X (3.0 m × 3.2 mm × 2.1 mm), with subsequent analysis by the TCD. For carbon-containing products such as CH_3OH, CH_3OCH_3 (dimethyl ether, DME), C_2H_4, C_2H_6, and C_3H_6, separation was conducted using another Porapak Q (PQ) column (2.0 m × 3.2 mm × 2.1 mm) and analysis via the FID. The external standard method was employed to quantify specific product contents, using standard gases with known concentrations as reference criteria. Product analysis was performed every 30 minutes for 6 h and on an hourly basis during long-term test (100 h).

The N_2O conversions were calculated according to Eq. S1.

$$X_{N_2O} = (1 - \frac{n_{outlet}}{n_{inlet}}) \times 100\% \tag{S1}$$

wherein n_{inlet} and n_{outlet} respectively represent the inlet and outlet molar content. The product generation rate (r_i) normalized to catalyst weight ($\mu mol\ g^{-1}\ h^{-1}$) were obtained according to Eq. S2 (except for the coke).

$$r_i = \frac{Y_i * F}{m_{cat}} \tag{S2}$$

, wherein Y_i represents the product yield; F is the total flow rate (μmol h^{-1}); and m_{cat} is the weight of catalyst sample (g).

The Y_i can be derived by Eq. S3

$$Y_i = \lambda \int A_i dt \tag{S3}$$

,wherein A_i represents the peak area of the product i detected by GC; λ is a calibration coefficient based on the external standard method. As noted, the reported product generation rates in main text of Fig. 1b and Fig. 1d are average value ($\bar{r}_i$) after 6 hour's test.

The product selectivity reported in Fig. 1e and Table S2 were respectively calculated according to Eq. S4 for the carbon-containing products (S_i) and Eq. S5 for the deposited carbon (S_C, coke), wherein the $\bar{r}_i$ is average value of product generation rate and r_C is deposited carbon generation rate which can be quantified according to the Eqs. S6-S7 based on the thermogravimetric analysis (TGA).

$$S_i = \frac{\bar{r}_i}{\sum_j \bar{r}_j + r_C} \tag{S4}$$

$$S_C = \frac{r_C}{\sum_j \bar{r}_j + r_C} \tag{S5}$$

$$r_C = \frac{\mathrm{n_{coke}}}{t \cdot \mathrm{m_{cat}}} \tag{S6}$$

$$\mathrm{n_{coke}} = \frac{\mathrm{m_{CO_2}} \cdot \mathrm{m_{cat}}}{13\mathrm{m_0}} \tag{S7}$$

The $\mathrm{n_{coke}}$ (mole) in Eq. S6 represents the amount of coke formed; t is the reaction duration; $\mathrm{m_{cat}}$ (g) is the catalyst weight utilized for the test. The $\mathrm{n_{coke}}$ can be calculated according to Eq. S7, wherein the $\mathrm{m_{CO_2}}$ (mole) represents the weight loss due to oxidation of deposited carbon to forming CO_2 during TGA; $\mathrm{m_0}$ (g) is the weight of catalyst sample utilized for the TGA; and 13 represents the molecular weight of coke by assuming C/H = 1.[1]

As reported,[2, 3] the large partial pressure of CH_4 in the gas stream prevents the accurate quantification of CH_4 consumption. Therefore, the CH_4 conversion (X_{CH_4}) was assumed to be equal to the total C-containing product (including the coke) divided by the initial molar flow rate of CH_4, as shown in Eq.S8.

$$X_{CH_4} = [\frac{(\sum_j r_j + r_C) \bullet m_{cat}}{F_{CH_4,0}}] \times 100\% \tag{S8}$$

Mechanism investigation based on in situ FTIR

In situ FTIR was also employed to investigate the N_2O mediated methane transformation mechanism (N_2O-DMTM, Fig. S9) as well as DME formation mechanism (Fig. 6d-6i) through interaction of CH_3OH with radicals of CH_3- and OH- over Cu-FER-0.3%. As for N_2O-DMTM mechanism, two experimental strategies were used: (i) co-feeding N_2O (2 vol% in He) and CH_4 (2 vol% in He) at a flow rate of 20 mL min^{-1} over Cu-FER-0.3% pretreated at 500 °C for 1 hour under a He atmosphere at 300 °C; (ii) introducing CH_4 (2 vol% in He) independently over N_2O-pretreated Cu-FER-0.3% to minimize the effect of H_2O on the generated OH- radicals' vibrations [*v*(OH)]. In the co-feeding experiment, mixed gases (2 vol% N_2O and 2 vol% CH_4, balanced with He for a total flow rate of 20 mL min^{-1}) were fed into a 3 mL tube connected to the microreactor via a needle valve, and IR spectra were recorded for 10 min after opening the valve. For the study of CH_4 interaction with N_2O-pretreated Cu-FER-0.3%, the catalyst was first treated with He at 500 °C for 1 hour, cooled to 300 °C, and then treated with N_2O (30 vol% in He, 40 mL min^{-1}) for another hour. The microreactor was subsequently purged with He (20 mL min^{-1}) for 15 min to remove residual N_2O. Finally, a CH_4 mixture (2 vol% in He) was introduced into the 3 mL tube, and spectra were recorded for 10 min after opening the needle valve.

As for the DME formation mechanism, similarly the Cu-FER-0.3% was initially pretreated He at 500 ^oC and then cooled down to 250 ^oC, with subsequent co-feeding of N_2O (2% in He) and CH_4 (2 in He) at flow rate of 20 mL min^{-1} for 10 min (signal recorded). After that, the sample was swept by He (>99.999%, 20 mL min^{-1}) and with the signal recorded for 10 min. Eventually, the CH_3OH, bubbled by He of 2 mL min^{-1} was introduced into the 3 mL tube. The IR spectra were recorded for 10 min after slightly open the valve.

Microkinetic modeling method

The microkinetic modeling was conducted in present work to illustrate reaction efficiency of monomeric $[Cu]^+$ (Table S5) Cu dimer (Table S6) and dual Cu SA (Table S7) sites to produce CH_3OH, as well as calculate the DME produce rate over Cu dimer site (Table 8) and monomeric $[Cu]^+$ (Table S9) site. The specific elementary reaction steps as well as the microkinetic parameters were listed in Tables S5-S9. The specific method can also be found in our previous work.[4] Specifically, the pre-exponential factors for the forward (v_{for}) and reverse reaction steps (v_{rev}) can be calculated based on the vibration frequencies of initial sate ($v_{\mathrm{m}}^{\mathrm{IS}}$), transition state ($v_{\mathrm{n}}^{\mathrm{TS}}$, saddle point) and final state ($v_{\mathrm{m}}^{\mathrm{FS}}$) according to the Eqs. S10-S11.[5] The reaction rate constant (*k)* can be further obtained according to the Arrhenius equation of Eq. S12,[6] wherein the *E* representing the energy barrier can be derived by DFT simulations.

$$v_{\mathrm{for}} = \frac{\prod_{\mathrm{m=1}}^{\mathrm{N}} v_{\mathrm{m}}^{\mathrm{IS}}}{\prod_{\mathrm{n=1}}^{\mathrm{N}} v_{\mathrm{n}}^{\mathrm{TS}}} \tag{S10}$$

$$v_{\mathrm{rev}} = \frac{\prod_{\mathrm{m=1}}^{\mathrm{N}} v_{\mathrm{m}}^{\mathrm{FS}}}{\prod_{\mathrm{n=1}}^{\mathrm{N}} v_{\mathrm{n}}^{\mathrm{TS}}} \tag{S11}$$

$$k = v\exp(-E / k_B T) \tag{S12}$$

As for the N_2O-DMTM over dual SA site by AIMD simulations, the reaction rate constant *k* was calculated according to the Eq. S13[7] based on the derived Gibbs free energy.

$$k = \frac{k_B T}{h}\exp(\frac{-\Delta G}{RT}) \tag{S13}$$

$$k_{\mathrm{ad}} = \mathrm{s_0} P_{\mathrm{i}} \mathrm{A_i} \Big/ \sqrt{2\pi \mathrm{m_i} k_{\mathrm{B}} T} \tag{S14}$$

As for the adsorption step, the adsorption rate constant k_{ad} was calculated based on Eq. S14,[7] wherein the $\mathrm{s_0}$ is the sticking coefficient of the adsorbates; P_{i} is the partial pressure (Pa) of species i; $\mathrm{m_i}$ is related molecular mass (kg); and $\mathrm{A_i}$ is the adsorption area ($\mathrm{m^2}$).

The coefficients s_0 for N_2O and CH_4 were estimated to be 0.02. The partial pressure of N_2O (P_{N_2O}), CH_4 (P_{CH_4}) was respectively set to be 30,397.5 (30 vol%) and 15,198.75 (15vol%) Pa according to the reaction condition of present work. The microkinetic modeling was solved based on a self-developed program by MATLAB, as elsewhere reported.[4]

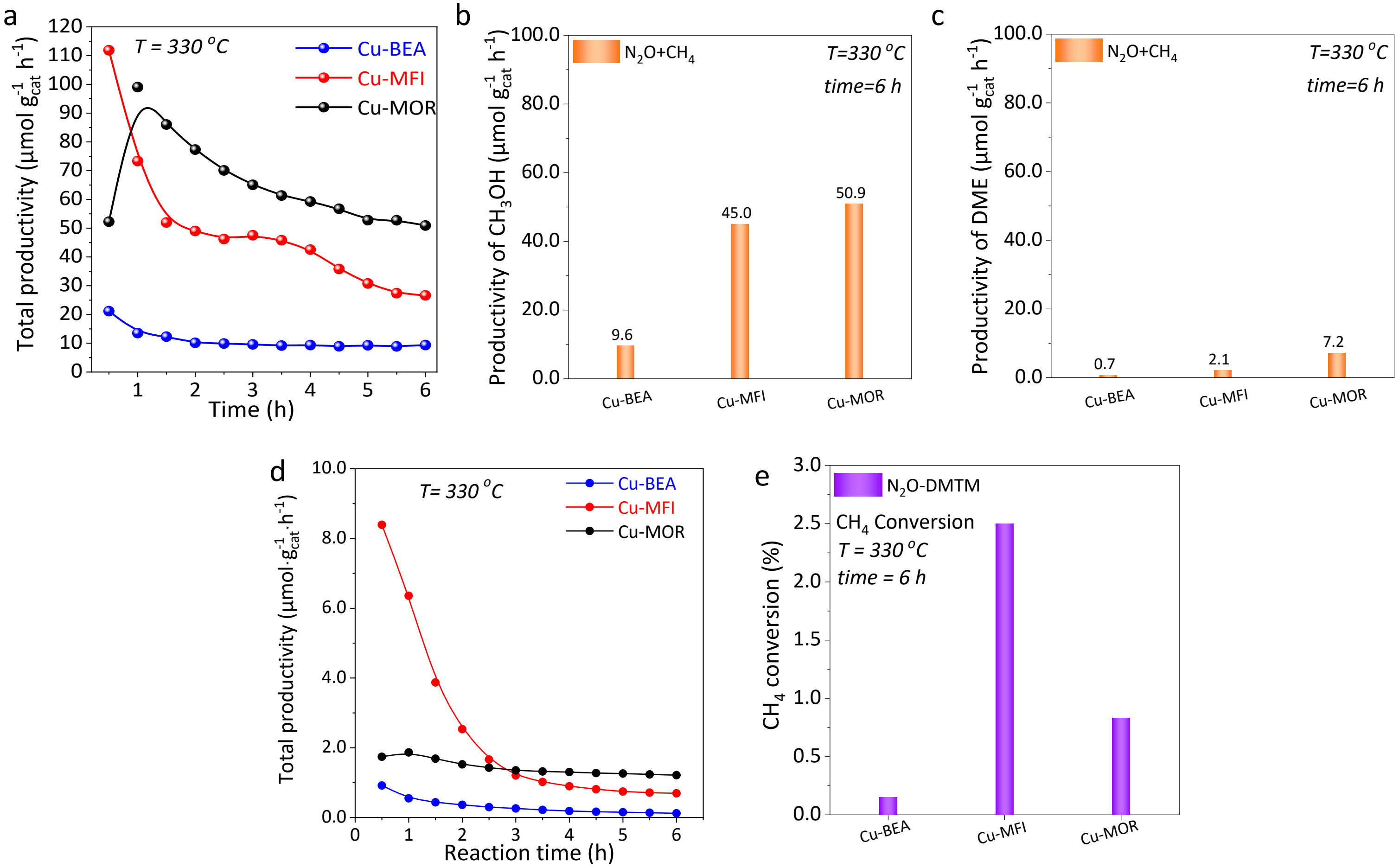

Fig. S1 Activity measurement (T = 330 °C, t = 6 h) result during N_2O-DMTM over Cu-Zeolites (BEA, MFI and MOR): (a) total productivity (CH_3OH + DME), (b) average CH_3OH productivity; (c) average DME productivity; (d) N_2O conversion; (e) average CH_4 conversion; reaction condition: N_2O: CH_4 : He = 30 : 15 : 55, gas hourly specific velocity (GHSV = 12,000 h^{-1}, m_{cat} = 0.5 g).

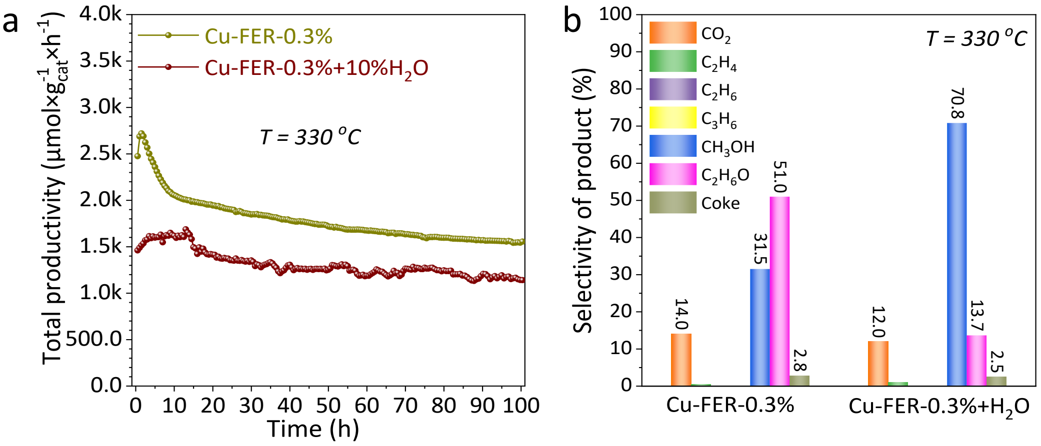

Fig. S2 Activity measurement result of total productivity (CH_3OH + DME) during (a) long term test of N_2O-DMTM over Cu-FER-0.3% in both presence and absence of H_2O (10 vol% H_2O); (b) the correlated reaction selectivity after 100 h's long term test for Cu-FER-0.3%; reaction condition: N_2O: CH_4: H_2O = 30: 15: 10 (0) : 45 (55), GHSV = 1,2000 h^{-1}, T = 330 °C; as noted, the total productivity of (CH_3OH + DME) in panel (a) and (b) is calculated by an equivalent weight of CH_3OH, wherein one mole DME is equivalent to two mole CH_3OH.

Note: The Cu-FER-0.3 exhibits excellent reaction stability, which can also display high CH_3OH productivity, ~1540 and 1140 μmol g_{cat}^{-1} h^{-1} for the scenarios of absence and presence of H_2O, even after 100 h's long-term reaction. On the contrary, the quick deactivation can be clearly observed for the samples of Cu-MFI and Cu-MOR (in panel c).

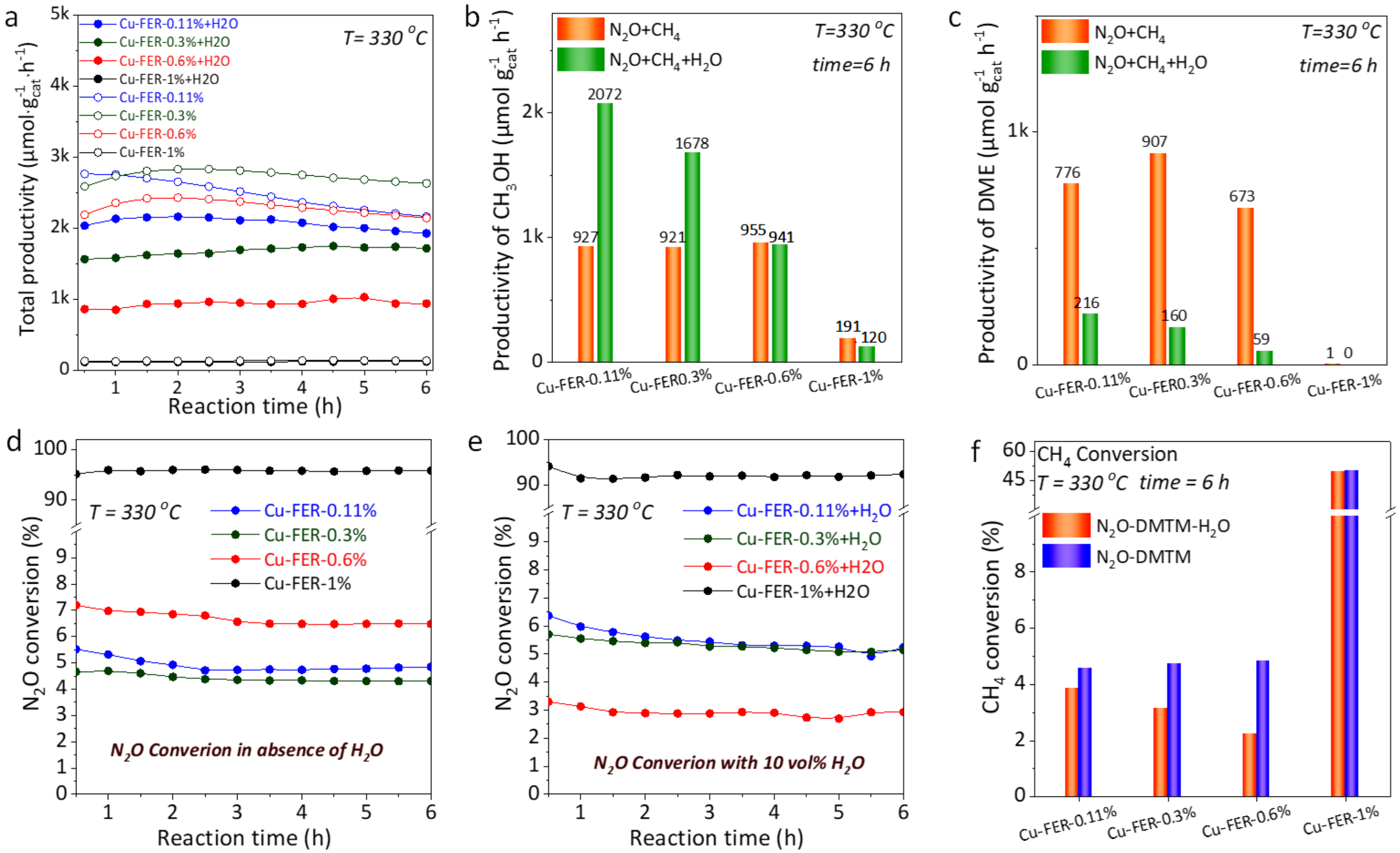

Fig. S3 Activity measurement results over Cu-FER samples with diverse Cu loadings (0.11, 0.3, 0.6 and 1%) in absence and presence of H_2O (10 vol%): (a) total productivity of (CH_3OH + DME) along with reaction time of 6 h; average value of (b) CH_3OH and (c) DME productivity after 6 h's reaction; (d) N_2O conversion of absence of H_2O; (e) N_2O conversion of presence of H_2O; (f) CH_4 conversion after 6 h's reaction; reaction condition: reaction condition: N_2O: CH_4 : He : (H_2O) = 30 : 15 : 55 (45): (10), gas hourly specific velocity (GHSV = 12,000 h^{-1}, m_{cat} = 0.5 g).

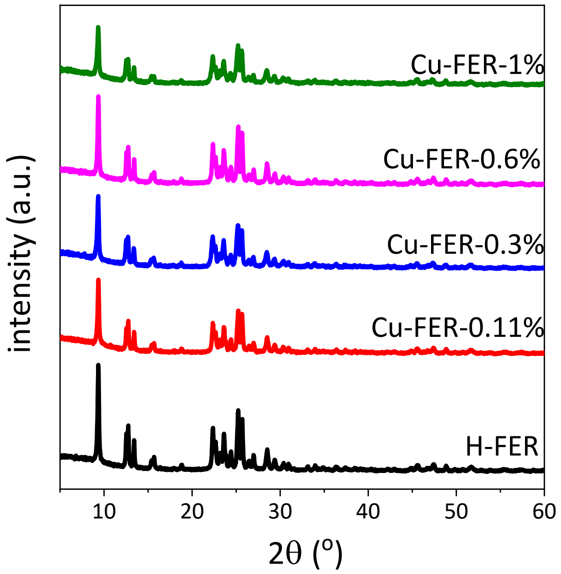

Fig. S4. XRD spectra of Cu-FER zeolite with diverse Cu loadings of 0.11-1.0wt.% and with H-FER as a reference.

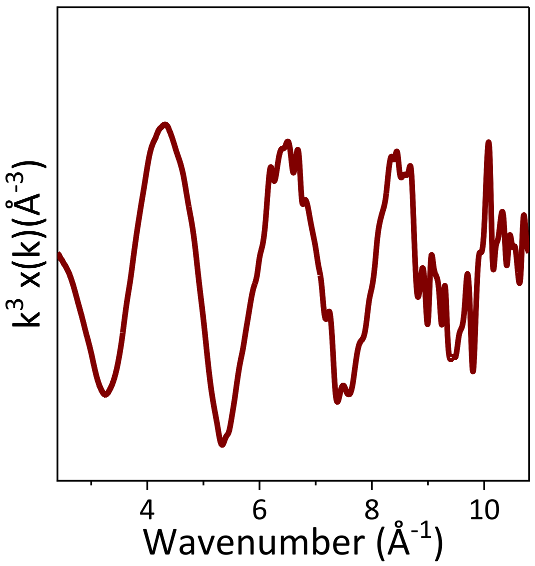

Fig. S5. k3χ(k) curve (2.4-10.8 Å) of Cu-FER-0.3% being after N_2O pretreatment at *T* = 250 ºC derived by XAS.

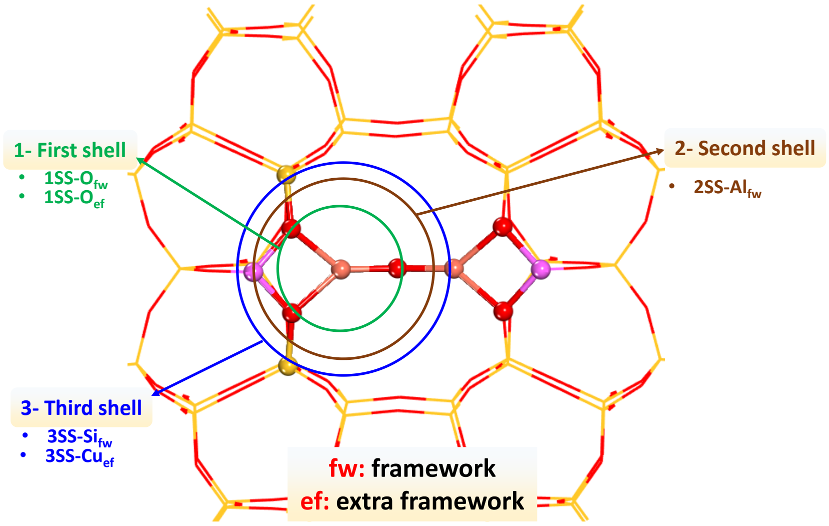

Fig. S6. DFT optimized Cu-FER model with oxo Cu dimer active site $[Cu\text{-}O\text{-}Cu]^{2+}$ site applied for the EXAFS peak fitting; orange Cu, red O, purple Al, yellow Si.

Note: Fig. S6 displays the DFT optimized Cu-FER model with oxo-Cu dimer site, which was utilized for the EXAFS peak fitting (Fig. 2i of the main text). The Cu was located at opposite T3 site of 10MR channel based on DFT energy calculation (see Fig. S7). The first shell is corresponding to single scattering (SS) of coordinated O atoms (two framework O, one extra-framework O); the second shell is related to SS of coordinated framework Al; and the third shell is contributed by SS of another Cu; the best fitting parameters is listed in Table S4.

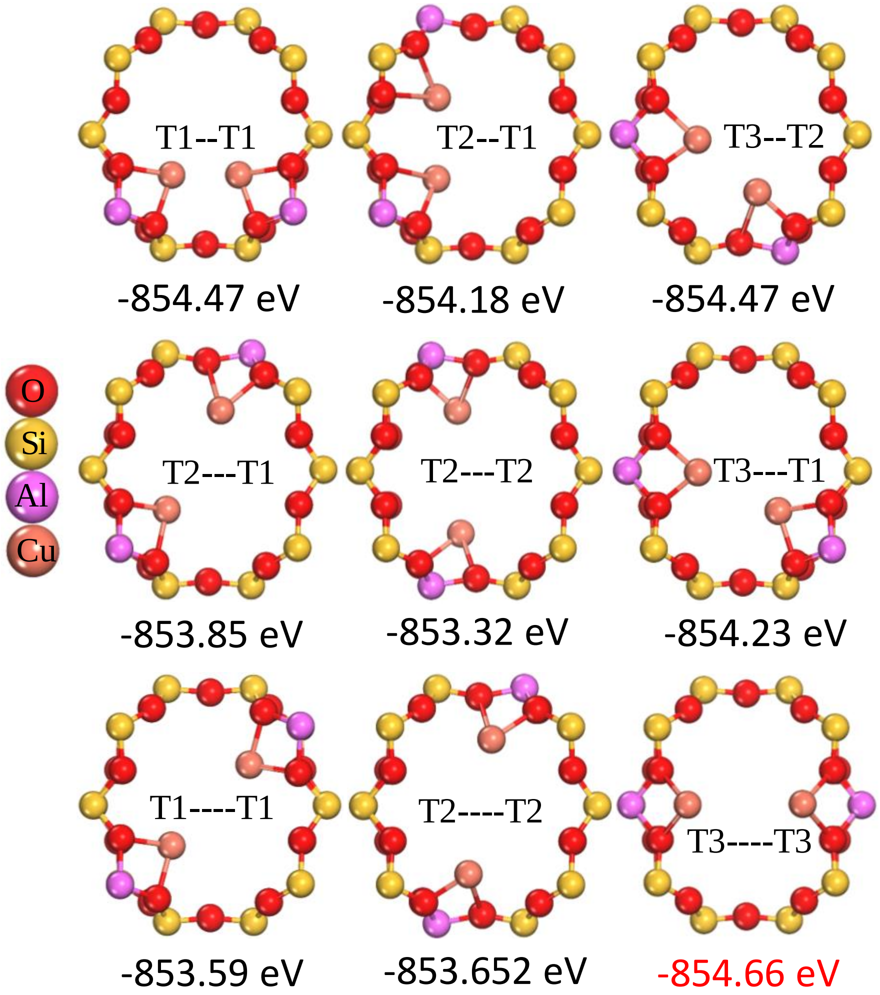

Fig. S7 Optimized Cu-FER models with Cu dimer active site. Diverse T sites have been screened, which indicates that the Cu dimer located at T3-T3 site exhibits lowest electric energy relative to other modes.

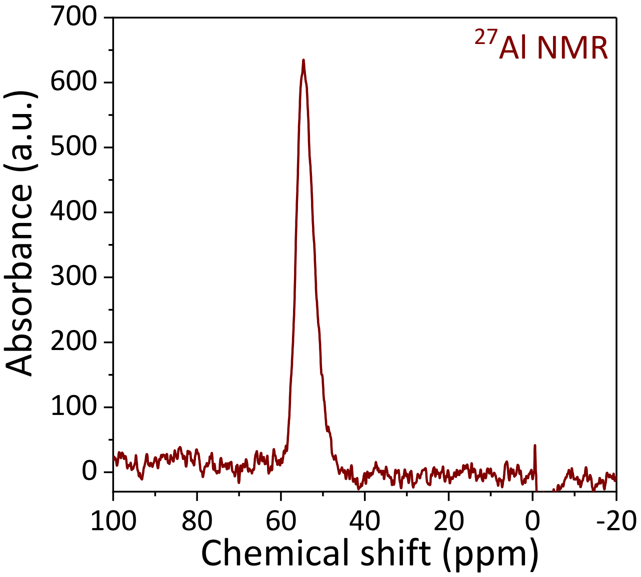

Fig. S8 27Al NMR spectra of Cu-FER-0.3%

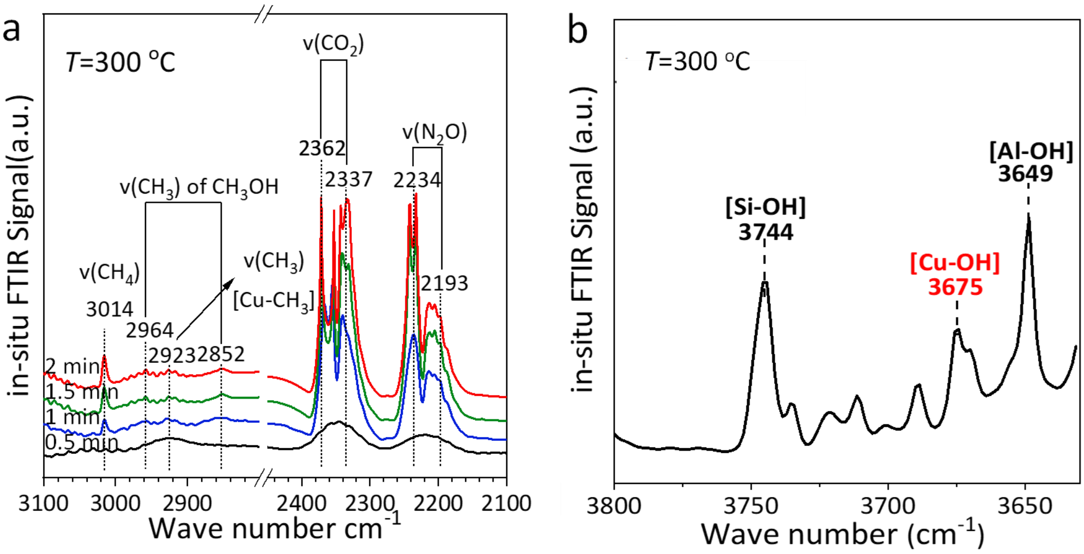

Fig. S9 In situ FTIR spectra of Cu-FER-0.3% under different conditions. (a) co-feeding of N_2O (2 vol%) and CH_4 (2 vol%) balanced by He of 20 mL min^{-1} at *T* of 300 °C along with time *t*. (b) Cu-FER-0.3% being initially pretreated by N_2O (*T* = 250 °C) and subsequently interacting with CH_4 (2 vol%, balanced by He of 20 mL min^{-1}). As noted, to avoid the influence of H_2O during Co-feeding of N_2O and CH_4, the in situ FTIR with Cu-FER-0.3% being initially pretreated by N_2O at 250 °C and subsequently interacting with CH_4 at 300 °C was conducted.

Note: In Fig. S9a, the characteristic vibration peak belonging to the radical of CH_3 generated over the Cu active site *v*[Cu-CH_3] can be clearly observed at 2923 cm^{-1} along with gradual increasing of the *v*(CH_3) belonging to CH_3OH at 2964 and 2852 cm^{-1}.[4] Additionally, the obvious vibration peak of the OH- radical ([Cu-OH])[4, 8] can also be detected by displaying the characteristic peak at 3575 cm^{-1} of Fig. S9b after Cu-FER-0.3% being pretreated by N_2O and subsequently interacting with CH_4. Combing these finding together, we can deduce that the CH_4 would follow the radical mechanism to produced CH_3OH over the Cu-FER-0.3%, wherein the CH_4 would be initially activated into the radicals of CH_3- and OH- which can be rebounded to form CH_3OH, as also proposed in our previous works.[4, 8]

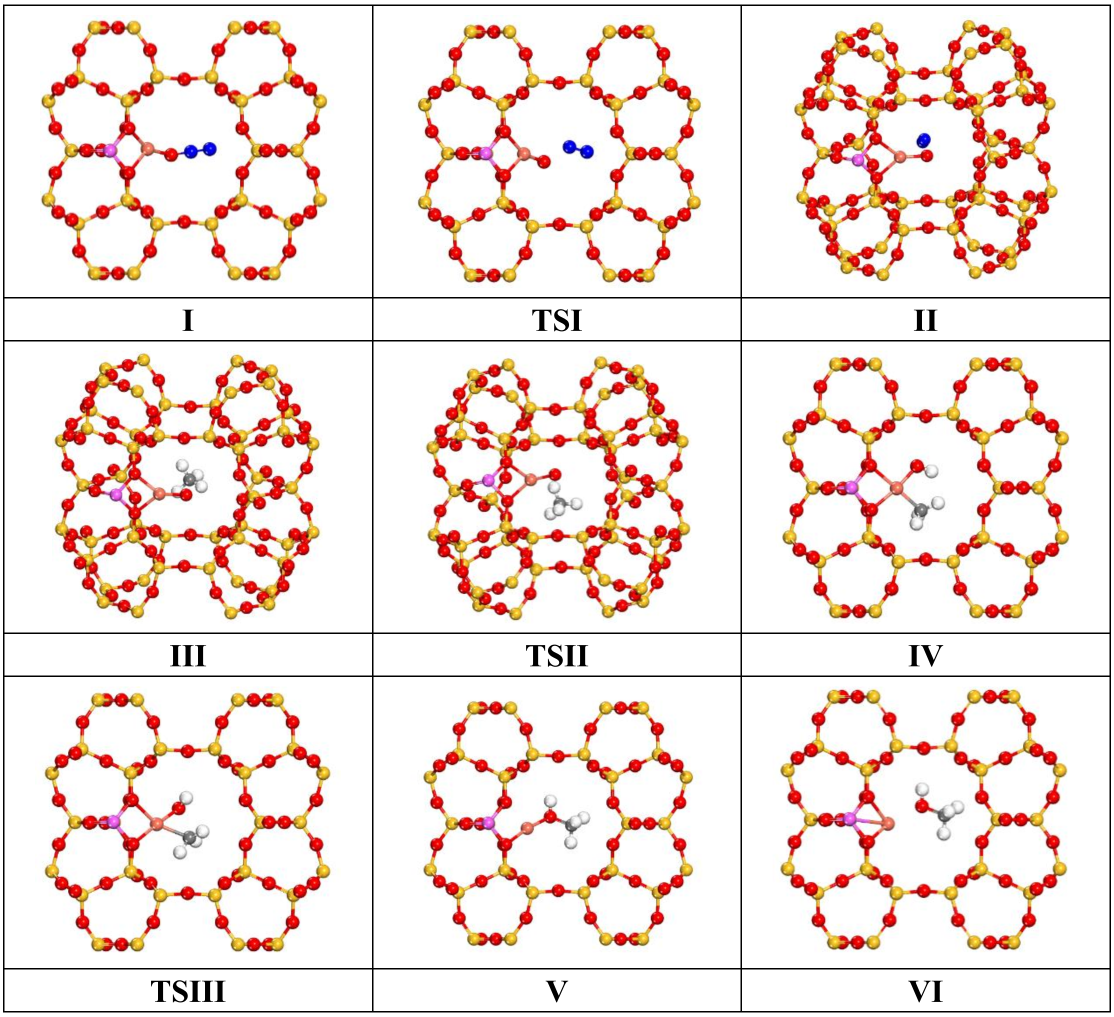

I TSI II

III TSII IV

TSIII V VI

Fig. S10 Optimized Cu-FER models with monomeric $[Cu]^+$ site during DFT mechanism simulation of N_2O-DMTM. The models were labeled according to the energy diagram of Fig. 3c.

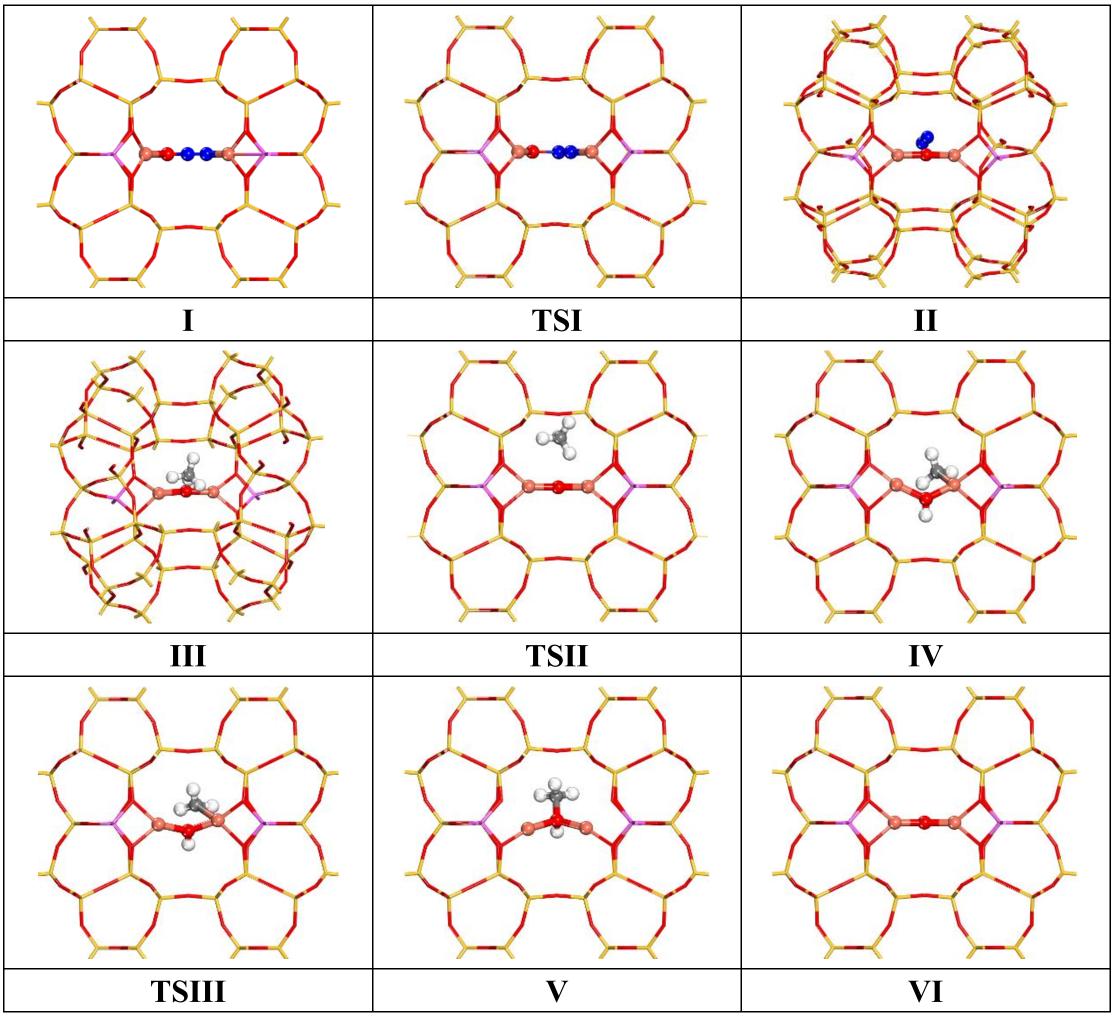

Fig. S11 Optimized Cu-FER models with Cu dimer active site during DFT mechanism simulation of N_2O-DMTM. The models were labeled according to the energy diagram of Fig. 3c.

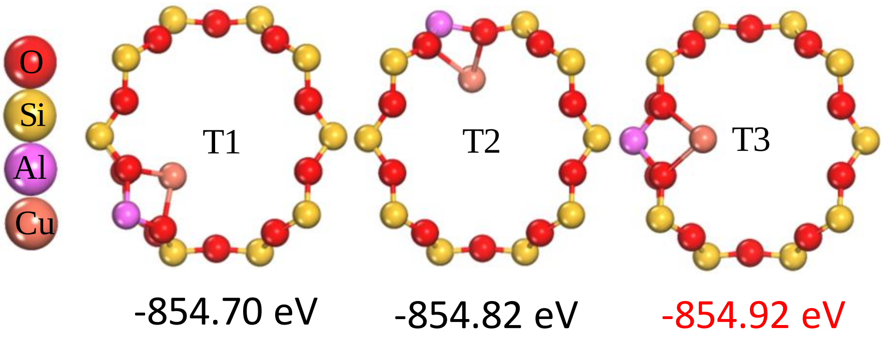

Fig. S12 Optimized Cu-FER models with monomeric $[Cu]^+$ being located at diverse T sites (T1-T3 sites) of 10 membered ring (MR) channel. The T3 site is chose as an optimum site for $[Cu]^+$ cation by displaying lowest electronic energy, relative to other T site.

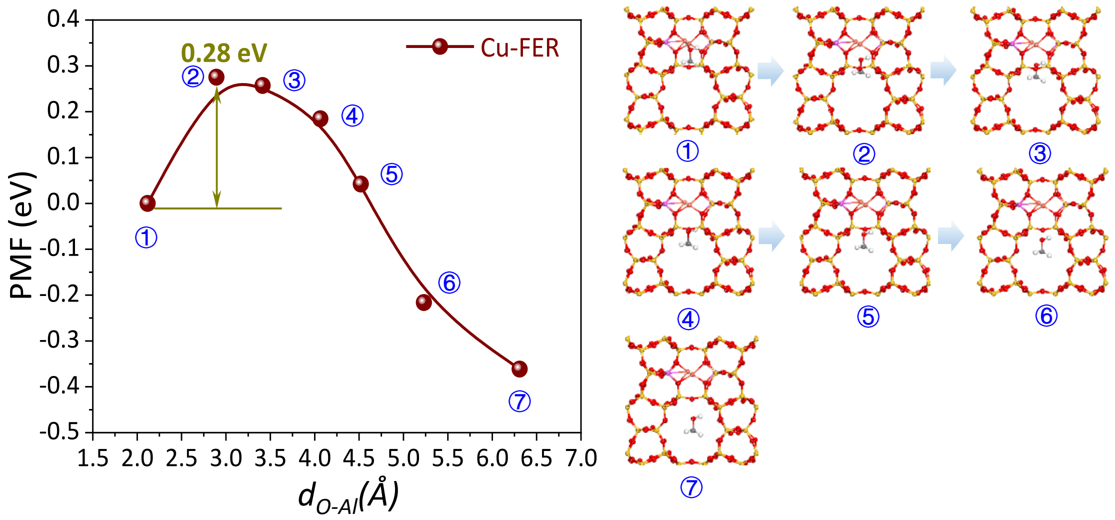

Fig. S13. Constrained MD simulation during CH_3OH diffusion from dual Cu SA site of 8 MR channel into 10 MR main channel of Cu-FER. The $d_{\text{O-Al}}$ represents the distance between framework Al and the atomic O of the diffusion molecule CH_3OH.

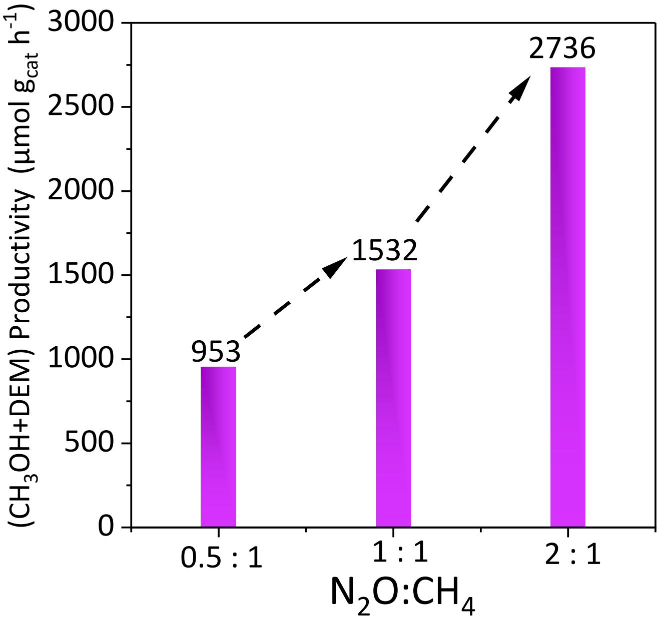

Fig. S14 (CH_3OH+DME) productivity comparison during N_2O-DMTM over Cu-FER-0.3% under divers (N_2O:CH_4) ratios of (0.5:1), (1:1) and (2:1) of T = 330 ºC, GHSV = 12,000 h^{-1}, CH_4 of 15 vol% in He.

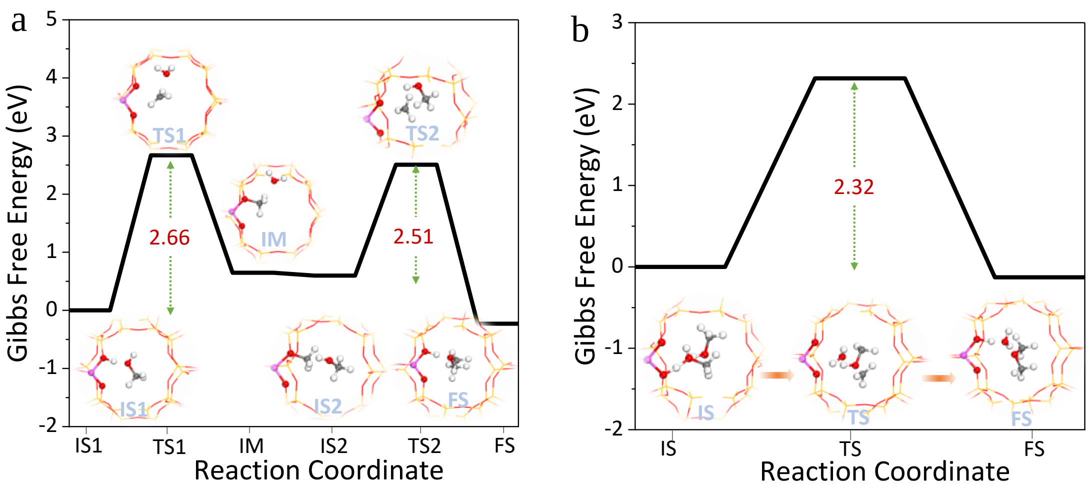

Fig. S15. DFT derived energy diagram of DME (a) sequential generation route; (b) associative generation route through the reaction of CH_3OH molecules over Brönsted acid site (BAS) and with the optimized models being inserted in the diagrams.

Note: As illustrated by DFT of Fig. S15a, in the sequential route the CH_3OH is initially adsorbed over the BAS and then activated into the radical of CH_3 by simultaneously releasing one molecule H_2O (ΔG = 2.66 eV, T = 330 ºC); subsequently, the second CH_3OH would interact with CH_3- to generate DME and renew the BAS site (ΔG = 2.51 eV, T = 330 ºC). However, the extremely high barriers makes such route being impossible under reaction condition of present work.

The associative routes, involving two CH_3OH molecules reacting over the BAS, were simulated by DFT (Fig. S15b), which, however, yielded a high barrier of 2.32 eV (ΔG, T = 330 ºC). Considering that the DFT simulation may not accurately depict the actual reaction process due to the complexity of the system involving two CH_3OH reactant molecules and one product molecule H_2O, the AIMD simulation (see Fig. 5 of main text) was thereby employed to unravel deeper insight.

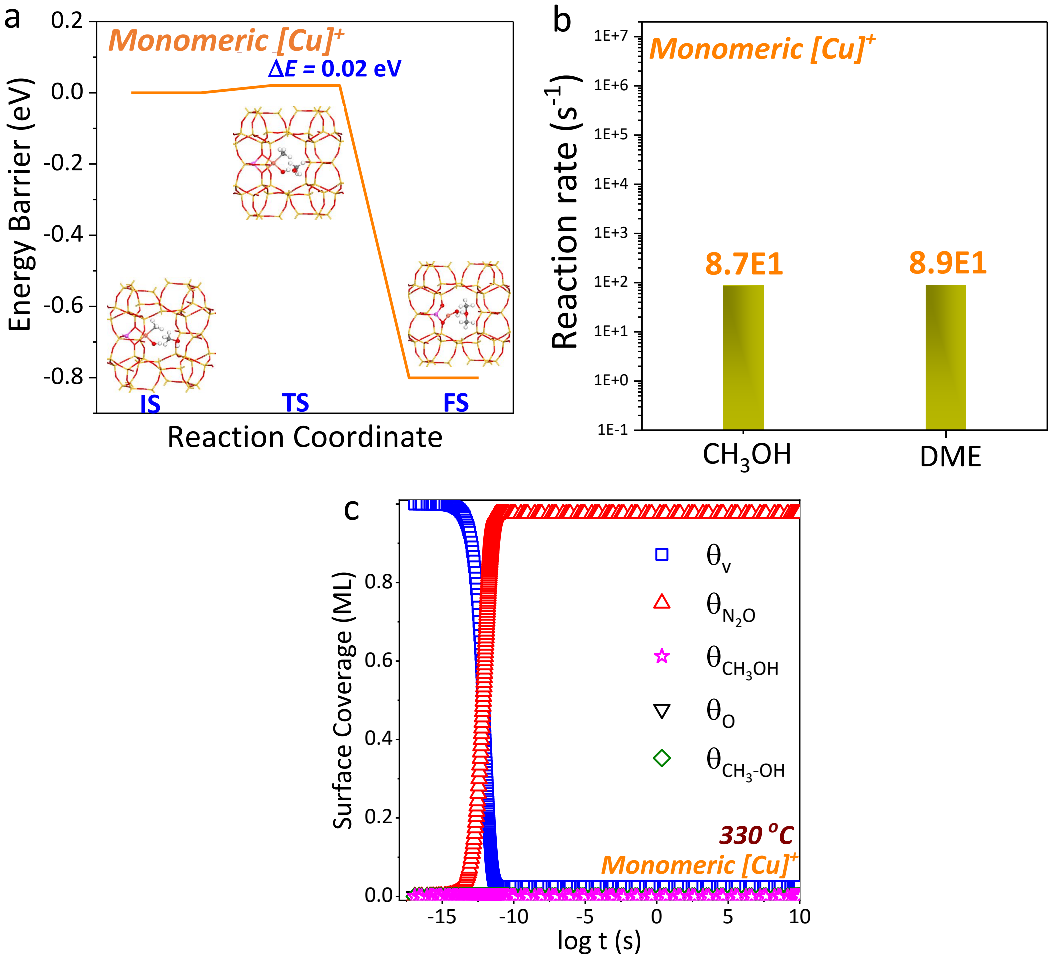

Fig. S16 DFT simulated DME generation route (CAS-DME) during N_2O-DMTM over Cu-FER and microkinetic modeling result. Derived energy diagram (a), CH_3OH/DME net reaction rate comparison (b) and surface coverage variations along with reaction time t (c) over monomeric [Cu]$^+$ site; O red, Cu orange, Al pink, Si yellow, C gray, H white. The optimized models involved the mechanism simulations were also detailedly profiled in Fig. S17(a-c).

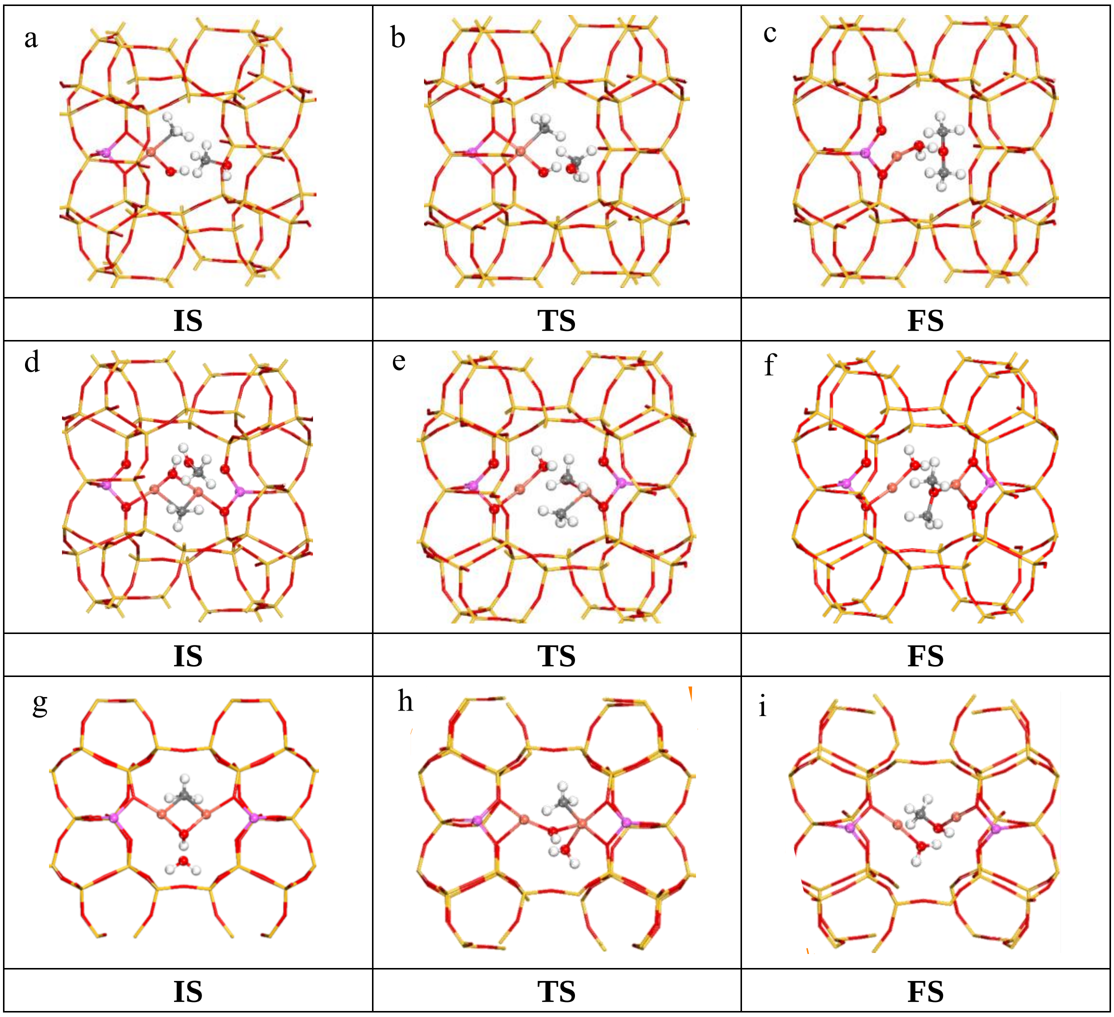

Fig. S17 Optimized models involved in DME generation mechanism simulations over (a-c) monomeric $[Cu]^+$ site, (d-f) Cu dimer site of 10 MR channel; and (g-i) optimized models involved in H_2O direct reaction with generated radicals of CH_3-and OH- over the Cu dimer site of Cu-FER. IS: initial state; TS: transition state; FS: final state.

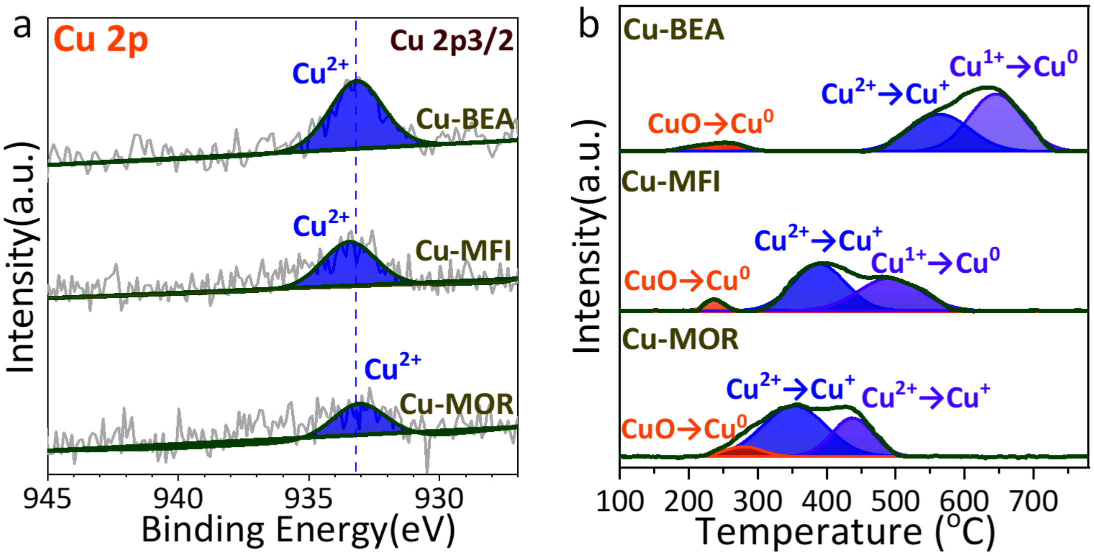

Fig. S18 (a) XPS spectra and (b) H_2-TPR of the samples of Cu-BEA, Cu-MFI and Cu-MOR with the Cu loading of 0.3wt%.

Note: Fig. S18a displays the XPS spectra of Cu 2P of Cu-Zeolite (BEA, MIF, MOR). It can be found that the Cu species would be majorly in 2+ valance state by displaying the Cu 2p 3/2 peak around 933.5 eV.[9] No obvious CuO species (936 eV)[4] can be observed, which indicates the well dispersion of the Cu species. The H_2-TPR of Fig. S18b further indicates minor CuO species would be generated over the Cu-Zeolite (BEA, MIF, MOR) by display a low H_2-TPR reaction peak around 200-300 ºC [10] and Cu^{2+} cation reaction peaks can be observed around 300-600 ºC for Cu-MOR, 350-600 ºC for Cu-MFI and 500-700 ºC for Cu-BEA. The different reaction peak regions can be closely correlated with the specific spatial structures of the Cu-Zeolite (BEA, MIF, MOR) and the Cu cation dispersed deep inside the internal channel of zeolite would be hard to be reduced.

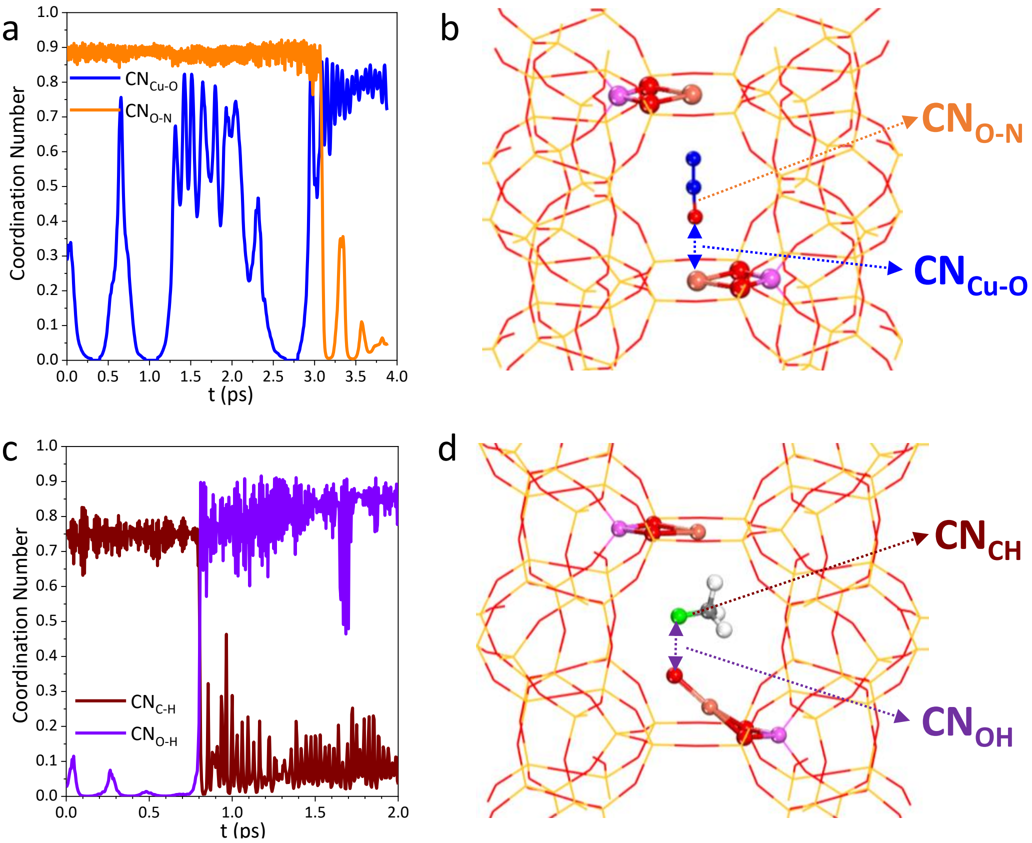

Fig. S19 Variations of coordination number (CN) along with the simulation time t during AIMD simulation of N_2O-DMTM over dual Cu SA site. (a) $CN_{Cu\text{-}O}$ & $CN_{O\text{-}N}$ corresponding to Fig. 4b, 4d of main text which respectively represents Cu-O bond and O-N bond of N_2O, as illustrated by panel (b); (c) $CN_{C\text{-}H}$ & $CN_{O\text{-}H}$ corresponding to Fig. 4c, 4e of main text which respectively represents the C-H bond of CH_4 and O-H bond of αO and dissociated atomic H, as illustrated in panel (d). As noted, the CN value being close to 1 represents bond formation which represents bond fracture when the value is close to 0; O red, Cu orange, Al pink, Si yellow, N blue, C gray, H, white; the dissociated atomic H of CH_4 was marked by green in Fig. S19d for the purpose of better displaying.

.

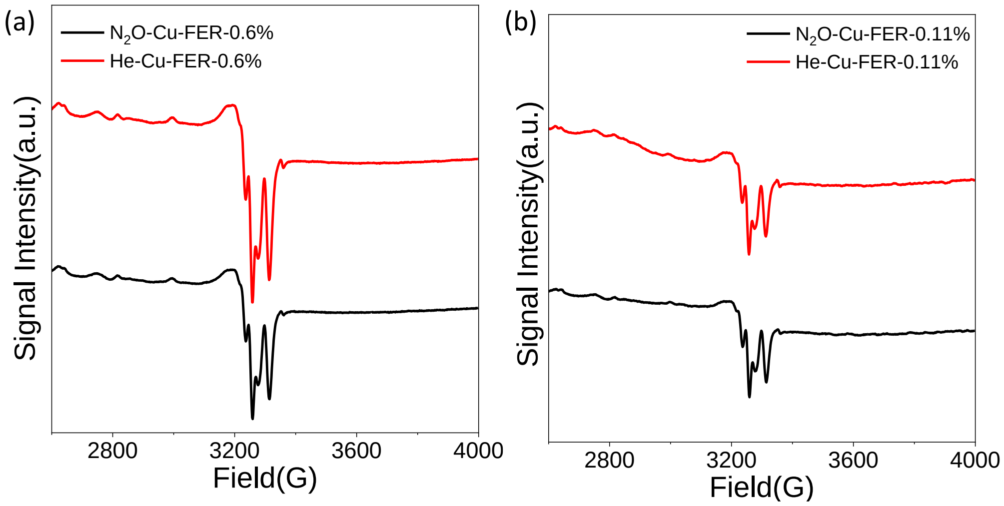

Fig. S20 EPR spectra of Cu-FER-0.11% and 0.6%, being respectively pretreated by He (500 °C, in He) and N_2O (350 °C by N_2O in He).

Note: The Cu dimer is estimated to respectively accounts for 25.4% and 18.5% of Cu over the Cu-FER-0.6% and Cu-FER-0.11% samples.

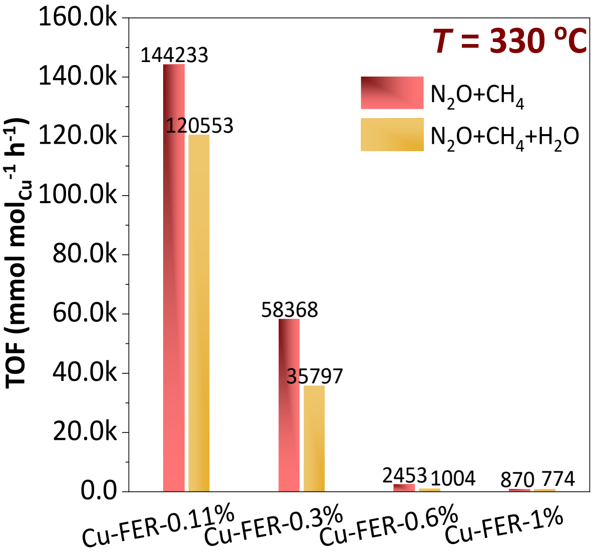

Fig. S21 Turn over frequency (TOF) of Cu-FER samples during N_2O-DMTM in absence and presence of H_2O; reaction conditions: reaction condition: N_2O: CH_4 : He : (H_2O) = 30 : 15 : 55 (45): (10), gas hourly specific velocity (GHSV = 12,000 h^{-1}, m_{cat} = 0.5 g).

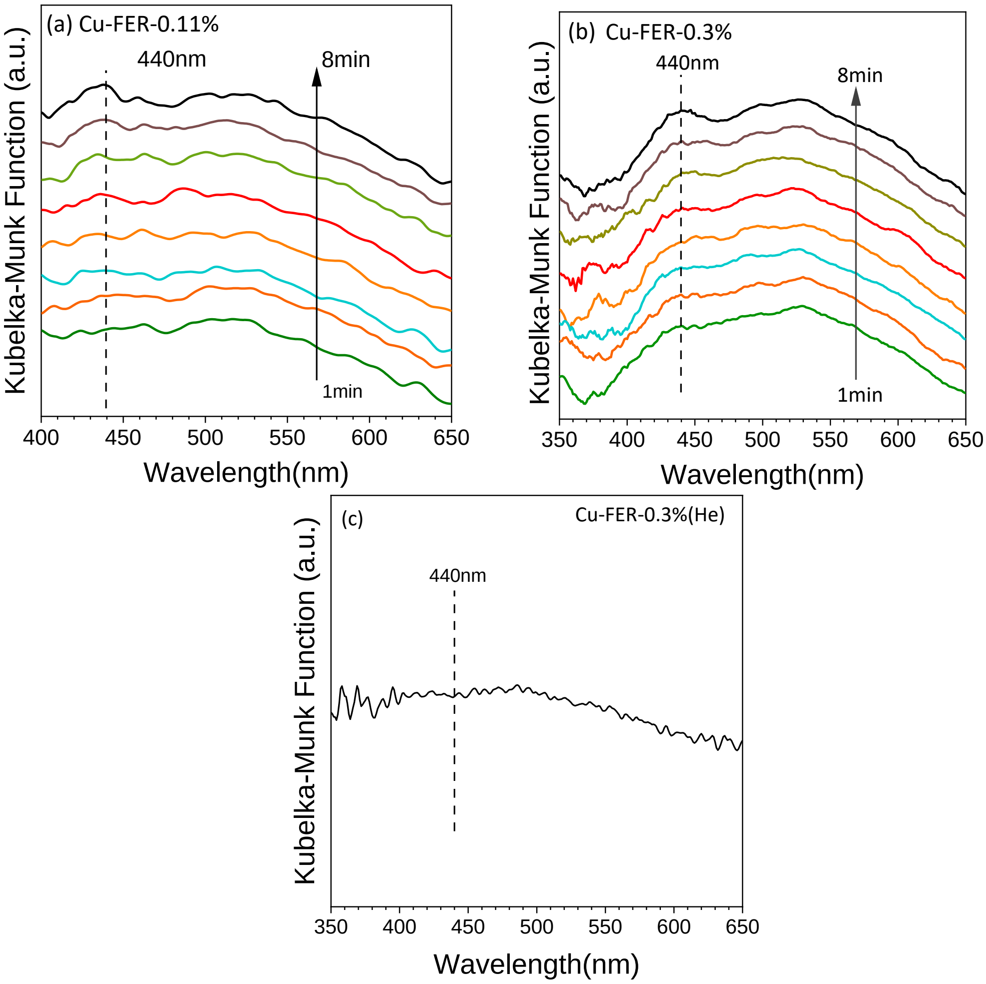

Fig. S22 in-situ UV-vis of (a) Cu-FER-0.11% and (b) Cu-FER-0.3% being pretreated by He (>99.999%) at *T* = 500 °C and subsequently interacting with N_2O (20 vol% in He, 20 mL min^{-1}) for 8 minutes at an interval of 1 minute; (c) in situ UV-vis of He-pretreated Cu-FER-0.3% taken as a reference.

Note: As shown in Figs. S22a-S22b, it displays the characteristic vibration peak at 440 nm for both the samples of Cu-FER-0.3% and Cu-FER-0.11%, which exactly verifies the formation of Cu dimer $[Cu\text{-}O\text{-}Cu]^{2+}$ active site after the N_2O pretreatment. Additionally, no obvious UV-vis peak around 440 nm can be observed over the He-pretreated sample of Cu-FER-0.33%, which can safely verify the generated peaks of 440 nm being related to the in situ formed $[Cu\text{-}O\text{-}Cu]^{2+}$.

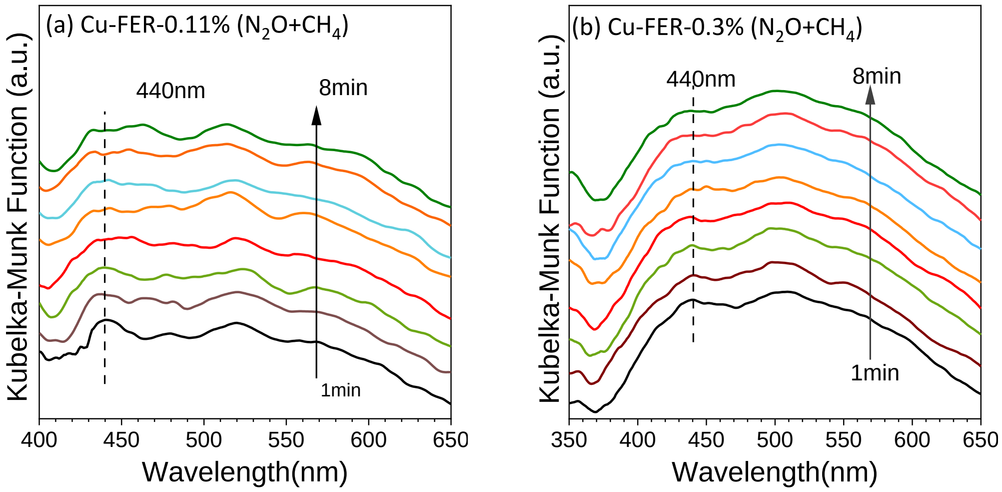

Fig. S23 in-situ UV-vis of (a) Cu-FER-0.11% and (b) Cu-FER-0.3% being pretreated by He (>99.999%) at *T* = 500 ºC and subsequently interacting with 30% N_2O /15% CH_4 / 55% He (100 mL min^{-1}) for 8 minutes at an interval of 1 minute.

Note: As shown in Figs. S23a-S24b, the characteristic vibration peak at 440 cm^{-1}, belonging to the [Cu-O-Cu]$^{2+}$ active site, can be observed, which gradually reduced along with reaction time *t*. This finding verified formation of Cu dimer active site during N_2O-DMTM.

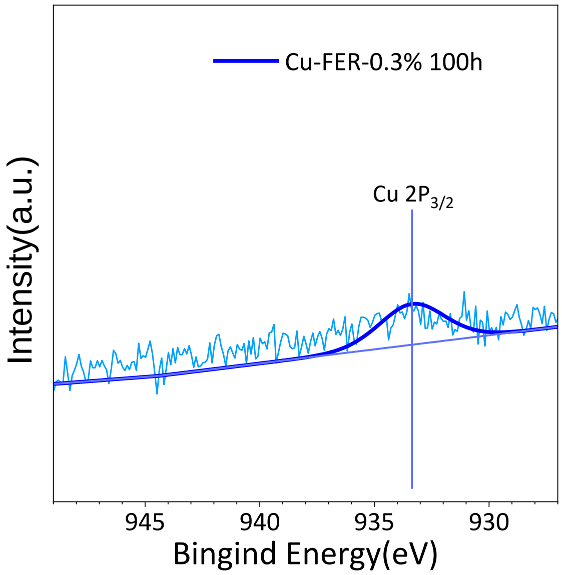

Fig. S24 XPS spectra of spent Cu-FER-0.3% after 100 h' reaction of N_2O-DMTM.

Note: The Cu species would maintain the Cu^{2+} cation state over the spent Cu-FER-0.3%

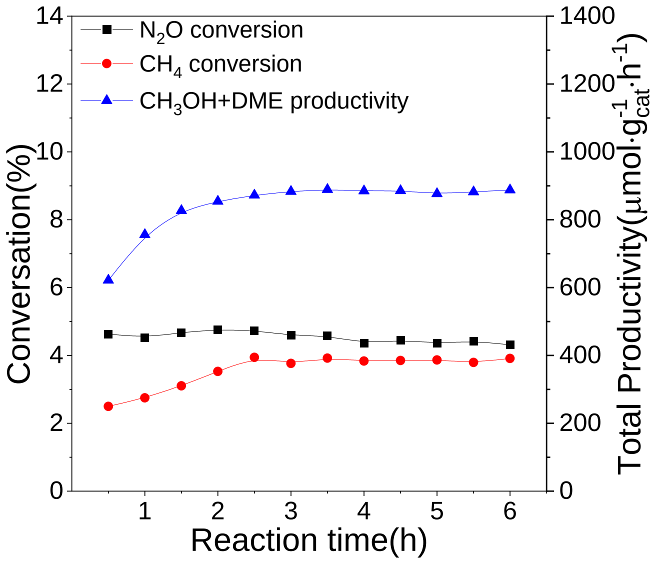

Fig. S25 N_2O-DMTM activity measurement over H-FER (SiO_2/Al_2O_3 = 30); reaction condition: N_2O: CH_4 : He = 30 : 15 : 55, gas hourly specific velocity (GHSV = 12,000 h^{-1}, m_{cat} = 0.5 g).

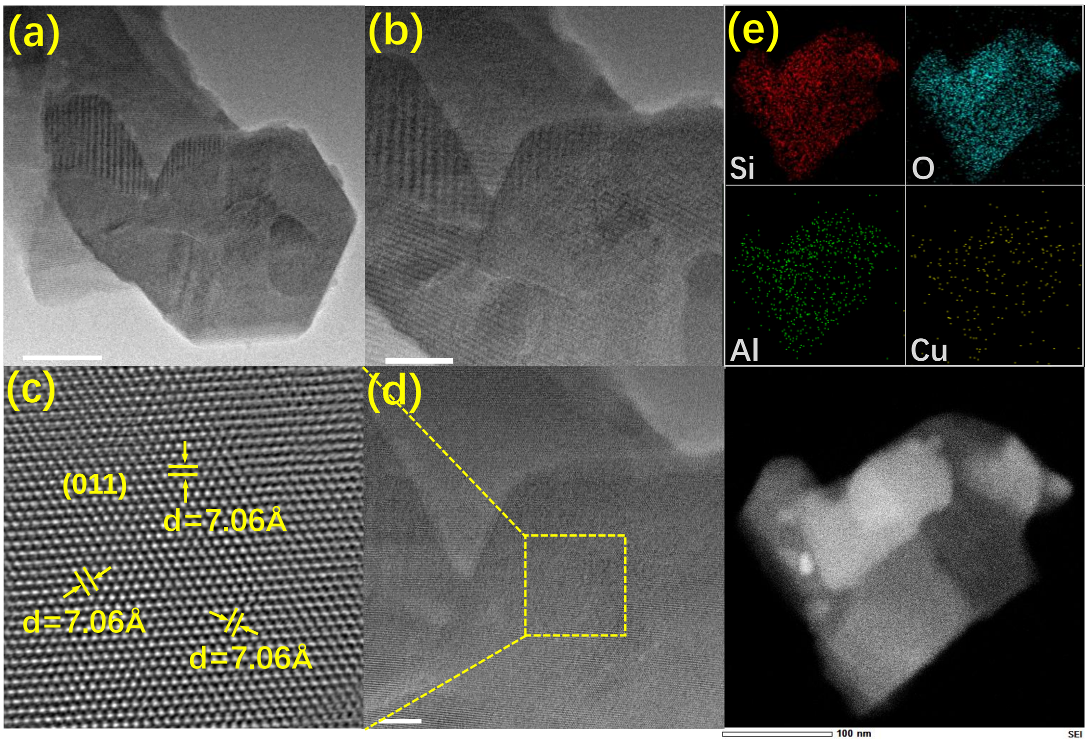

Fig. S26 HRTEM (a-d) and EDS mapping results of the spent Cu-FER-0.3% (after 100 h's reaction)

Note: The crystal structure is also well preserved and eventually dispersed Cu can also be observed for the sample of Cu-FER-0.3 after 100 h's long-term test.

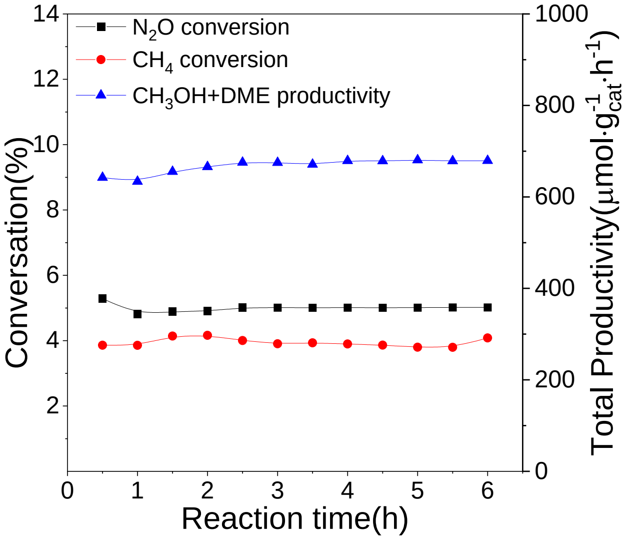

Fig. S27 N_2O-DMTM activity measurement result over Cu-FER-0.3% with a SiO_2/Al_2O_3 ratio of 70; Reaction condition: reaction condition: N_2O: CH_4 : He = 30 : 15 : 55, gas hourly specific velocity (GHSV = 12,000 h^{-1}, m_{cat} = 0.5 g).

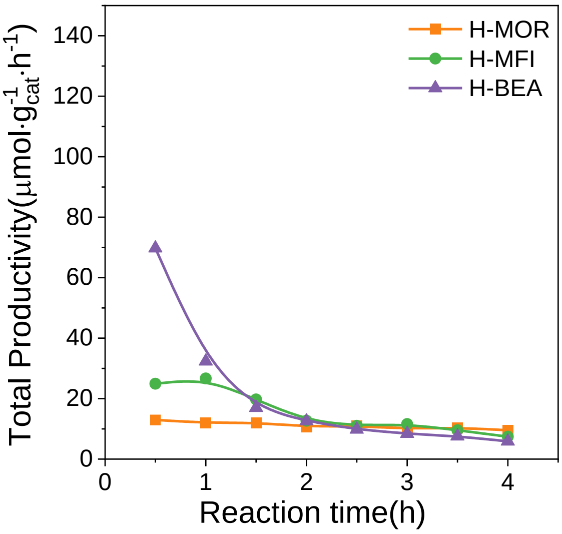

Fig. S28 N_2O-DMTM activity measurement over H-MOR, H-MFI and H-MOR (SiO_2/Al_2O_3 = 30); reaction condition: N_2O: CH_4 : He = 30 : 15 : 55, gas hourly specific velocity (GHSV = 12,000 h^{-1}, m_{cat} = 0.5 g).

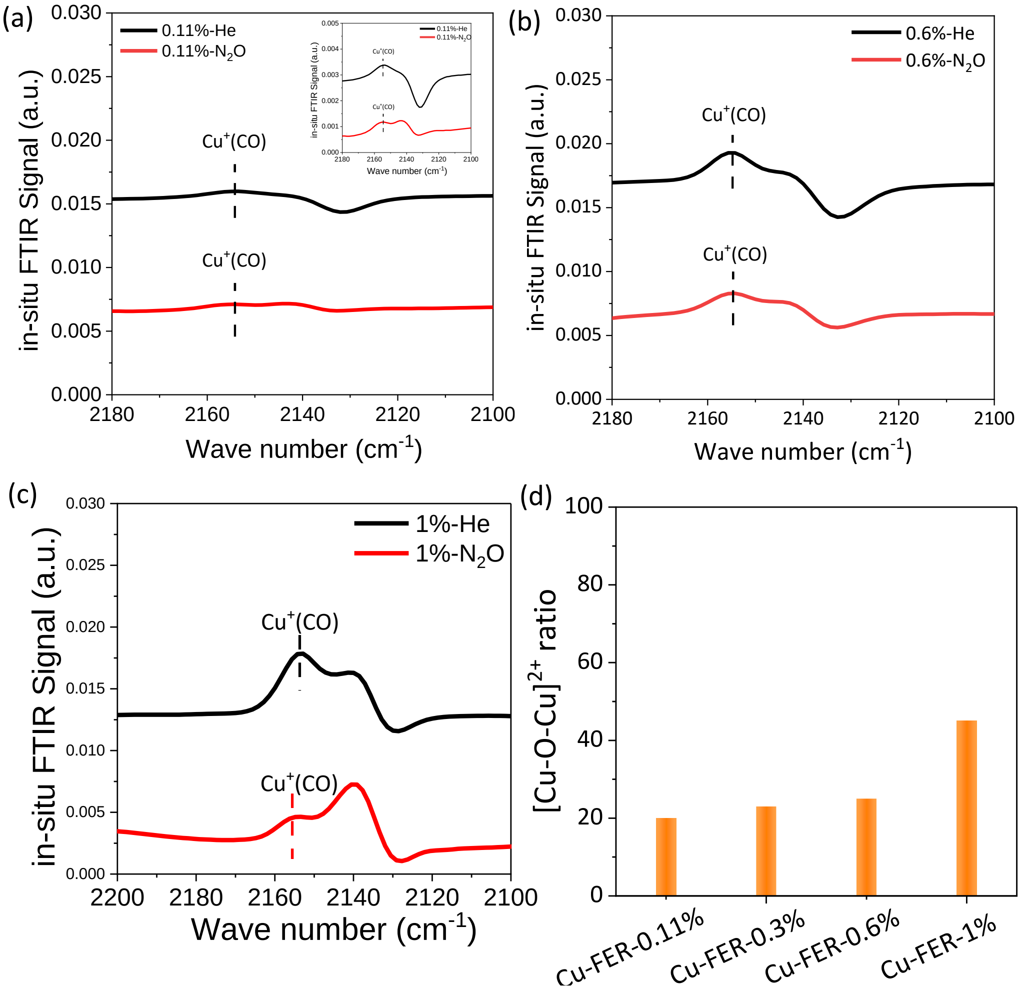

Fig. S29 CO probed in situ FTIR over (a) Cu-FER-0.11%, (b) Cu-FER-0.6%, (c) Cu-FER-1% and (d) estimated [Cu-O-Cu]$^{2+}$ ration based on panel (a), (b), (c) and Fig. 2c.

Note: As can be seen, the estimated values (through peak area integration) were comparable to those predicated by EPR (see Table S14), indicating lower amounts of generated Cu dimer site [Cu-O-Cu]$^{2+}$ over Cu-FER-0.11%, Cu-FER-0.3% and Cu-FER-0.6%.

Table S1 Activity comparisons of continuous DMTM with literature report

No.	Sample	CH_3OH Productivity (mmol molM^{-1} h^{-1}) (M=Cu、Fe、Au etc.)	CH_3OH Selectivity (%)	Reaction Conditions	Oxidant	Refs.
1	Cu-SSZ-13	543	91	T=300°C; m_{cat}=0.1g; 98%CH_4, 2%H_2O, 400ppmO_2; GHSV=36000 mL h^{-1} gcat^{-1}	O_2	[11]
2	Cu-SSZ-13	37.6	95	T=270°C; m_{cat}=0.25g; P_{CH4}=18kPa, P_{H2O}=3.14kPa, P_{O2}=0.09kPa, balanced by He	O_2	[12]
3	Cu-Fe-SSZ-13	188.3	91	T=200 °C; m_{cat}=0.05g; 10vol%CH_4, 2vol%H_2O, 400ppmO_2, balanced by Ar; flow rate=60 mL min^{-1}	O_2	[13]
4	Cu-MOR	15	58	T=300°C; m_{cat}=0.1g; 98%CH_4, 2%H_2O, 400ppmO_2; GHSV=36000 h^{-1}	O_2	[11]
5	Fe/UiO-66	11.9	62	T=180 °C; m_{cat}=0.17g; P=5 bar; 10%CH_4, 0.2%H_2O, 5%O_2, balanced by Ar; flow rate=30 mL min^{-1}; GHSV=6285 h^{-1}	O_2	[14]
6	Cu-SSZ-39	26.9	80	T=225°C; m_{cat}=0.4g; 50% CH_4, 2% water, 250 ppm O_2; flow rate=40 mL min^{-1} ; WHSV=6000mL h^{-1} gcat^{-1}	O_2	[15]

7	Cu-KFI	880.3	83	T=450°C; m_{cat}=0.1g; 90%CH_4, 3.2%H_2O, 100ppmO_2; GHSV=9000 ml g_{cat}^{-1} h^{-1}	H_2O O_2	16
8	Cu-SSZ-13	10.9	-	T=225°C; m_{cat}=0.25g; P_{CH4}=49.5kPa, P_{H2O}=2.3kPa, P_{O2}=0.025 kPa, balanced by He; WHSV=6000mL h^{-1} $gcat^{-1}$	H_2O	17
9	Cu_1/γ-Al_2O_3	47	85	T=200 °C; m_{cat}=0.1g; 90%CH_4, 3.2%H_2O, balanced by He; flow rate=15mL min^{-1}	H_2O	18
10	Cu-Na-MOR	5.8	89.7	T=350°C; m_{cat}=0.8g; 33%CH_4, 67%H_2O; flow rate=240 mL min^{-1}; WHSV=18000mL h^{-1} $gcat^{-1}$	H_2O	19
11	Cu-SSZ-13	578.7	91	T=350°C; m_{cat}=0.1g; 90%CH_4, 3.2%H_2O, balanced by He; flow rate =15 mL min^{-1}	H_2O	20
12	Cu_1-SSZ-13	2678	93	T=400°C; m_{cat}=0.1g; 90% CH_4 , 3.2% H_2O, balanced by He;; flow rate=15mL min^{-1}	H_2O	21
13	Au-Fe-HS	595	95	T=80°C; m_{cat}=0.1g; 20mL $min^{-1}$$CH_4$, 2mL h^{-1} H_2O_2,	H_2O_2	22

14	Cu-SSZ-13	23272.7	80	T=300°C; m_{cat}=0.3g; CH_4:N_2O:H_2O=30:30:3, balanced by He; flow rate=120mL min^{-1}; WHSV=19650 h^{-1}	N_2O	[23]
15	Cu-SSZ-39	1024	34	T=300°C; m_{cat}=0.3g; P_{CH4}=40.5kPa, P_{N2O}=10.1kPa, P_{H2O}=2.6kPa; GHSV = 10400 h^{-1}	N_2O	[24]
16	Fe-MOR	1160.7	47	T=300°C; m_{cat}=0.3g; 30%CH_4, 10%N_2O,22-24%H_2O, Balanced by He; GHSV=13000 h^{-1}	N_2O	[25]
17	Fe-FER	1592.5	71	T=300°C; m_{cat}=0.3g; 30%CH_4, 10%N_2O,22-24%H_2O, Balanced by He; GHSV=13000 h^{-1}	N_2O	[25]
18	Fe-ZSM-5	4240.8	52	T=300°C; m_{cat}=0.3g; 30%CH_4, 10%N_2O, 22-24%H_2O, Balanced by He; GHSV=13000 h^{-1}	N_2O	[25]
19	Cu-BEA	2590.9	71.6	T=320°C; m_{cat}=0.5g; CH_4:N_2O:H_2O:He=15:30:10:45; flow rate=100mL min^{-1}; GHSV=12000 h^{-1}	N_2O	[4]
20	Cu/AEI	13888	50	T=350 °C; m_{cat}=0.1g; CH_4:N_2O:H_2O:Ar= 10:10:2:3 mL min^{-1}; WHSV=15000 ml g^{-1} h^{-1}.	N_2O	[26]

21	Cu/AEI	15556	45	T=350 ºC; m_{cat}=0.1g; $CH_4:N_2O:H_2O:Ar$ = 10:10:2:3 mL min^{-1}; flow rate=15 mL min^{-1}; WHSV=15000 mL g^{-1} h^{-1}	N_2O	[27]
22	**Cu-FER**	**27375**	**78**	**T=300℃;** **m_{cat}=0.5g;** **$CH_4:N_2O:He$=15:30:55;** **flow rate=100mL min^{-1};** **GHSV=12,000 h^{-1}**	N_2O	**Present work**
23	**Cu-FER**	**58368**	**80.3**	**T=330℃;** **m_{cat}=0.5g;** **$CH_4:N_2O:He$=15:30:55;** **flow rate=100mL min^{-1};** **GHSV=12,000 h^{-1}**	N_2O	**Present work**

Table S2 Product selectivity of investigated Cu-FER samples with diverse Cu loading during continuous N_2O-DMTM in absence and presence of H_2O under *T* of 330 °C

Sample	t(h)	Selectivity (%)							
		CO_2	C_2H_4	C_2H_6	C_3H_6	CH_3OH	DME	Coke	(CH_3OH+ DME)
[a]Cu-FER-0.11%	6	6.5	0.4	0.1	0.1	28.1	47.0	17.8	75.1
[a]Cu-FER-0.3%	6	5.1	0.4	0.1	0.1	26.9	53.1	14.3	80.3
[a]Cu-FER-0.6%	6	19.5	0.6	0.1	0.1	26.8	37.8	15.0	64.6
[a]Cu-FER-1%	6	99.1	0	0	0	0.4	0	0.4	0.4
[a]Cu-FER-0.3%	100	14.0	0.5	0.1	0.1	31.5	51.0	2.8	82.5
[b]Cu-FER-0.11%+H_2O	6	8.6	1.2	0.1	0.1	59.0	15.6	15.5	74.6
[b]Cu-FER-0.3%+H_2O	6	11.5	1.2	0	0.1	59.4	13.9	13.8	73.4
[b]Cu-FER-0.6%+H_2O	6	30.0	1.1	0	0	52.8	7.6	8.4	60.4
[b]Cu-FER-1%+H_2O	6	99.2	0	0	0	0.3	0	0.4	0.3
[b]Cu-FER-0.3%+H_2O	100	12.0	1.0	0	0.1	70.8	13.7	2.5	84.5

[a] N_2O-DMTM

[b] N_2O-DMTM-H_2O (10vol% H_2O)

Table S3 Quantitative analysis of H_2-TPR over Cu-FER samples

Samples	Peak position (°C)	Species	[a]H_2 consumption (μmol·g^{-1})	[b]Cu content (μmol·g^{-1})	[b]Cu content (wt%)
Cu-FER-0.11%	459	Cu^{2+} cation	8.9	17.8	0.11
Cu-FER-0.3%	463	Cu^{2+} cation	23.6	47.2	0.30
Cu-FER-0.6%	283	dispersed CuO	30.3	30.3	0.19
	379	CuO cluster	25.6	25.6	0.14
	448	Cu^{2+} cation	18.8	37.6	0.24
Cu-FER-1%	268	dispersed CuO	76.2	76	0.49
	380	CuO cluster	23.6	23.6	0.15
	448	Cu^{2+} cation	24.6	49.2	0.31

[a]H_2 consumption was predicted based on the stand CuO

[b]Cu content predicted by H_2 consumption

Note: The Cu content (last column) predicate by H_2 consumption fits well with the Cu content determined by ICP, which verifies the deconvolution of H_2-TPR.

Table S4 EXAFS Peak-fitting parameters for Cu-FER pretreated by N_2O at $T = 250$ °C

Path	N	R	σ^2(Å^2)	R-factor	ΔE_0 (eV)
Cu-O_{ef}	1.0	1.82 (±0.011)	0.00312	0.0022	1.470 ± 0.6
Cu-O_{fw}	2.0	1.96 (±0.009)	0.00206	0.0022	1.470 ±0.6
Cu-Al_{fw}	1.0	2.97 (±0.051)	0.01057	0.0022	1.470 ±0.6
Cu-Si_{fw}	2.0	3.28 (±0.056)	0.02409	0.0022	1.470 ±0.6
Cu-Cu_{ef}	1.0	3.38 (±0.056)	0.02409	0.0022	1.470 ±0.6

Note: N is the coordination number; R is interatomic distance; σ^2 is Debye-Waller factor; ΔE_0 is inner potential correction; R-factor indicates the goodness of the fit; S_0^2 fixed as 0.90; Data ranges: $2.4 \leq k \leq 10.8$ Å^{-1}, $1 \leq R \leq 3.8$ Å.

Table S5. Elementary steps and kinetic parameters involved in microkinetic modeling over monomeric $[Cu]^+$ site of Cu-FER during N_2O-DMTM

Step	Elementary Steps	Reaction rate equations	[a]ν_{for} (s^{-1})	[b]ν_{rev}^{-1} (s^{-1})	ΔE (eV)	ΔE^{-1} (eV)
R1	$\text{Z-Cu} + N_2O(g) \leftrightarrow \text{Z-Cu-}N_2O$	$r_1 = k_1{}^{c}P_{N_2O}\theta_v - k_{-1}\theta_{N_2O}$	0.02	2.09E10	-	0.33
R2	$\text{Z-Cu-}N_2O \leftrightarrow \text{Z-Cu-O} + N_2(g)$	$r_2 = k_2\theta_{N_2O}$	1.78E13	-	1.35	-
R3	$\text{Z-Cu-O}+CH_4(g) \leftrightarrow \text{Z-Cu-}CH_3\text{-OH}$	$r_3 = k_3{}^{d}P_{CH_4}\theta_O - k_{-3}\theta_{CH_3-OH}$	3.18E12	2.81E14	0.12	1.71
R4	$\text{Z-Cu-}CH_3\text{-OH} \leftrightarrow \text{Z-Cu-}CH_3OH$	$r_4 = k_4\theta_{CH_3\text{-OH}} - k_{-4}\theta_{CH_3OH}$	6.58E12	2.49E13	0.42	1.27
R5	$\text{Z-Cu-}CH_3OH \rightarrow \text{Z-Cu} + CH_3OH(g)$	$r_5 = k_5\theta_{CH_3OH}$	2.11E10	1.12	-	-

[a] pre-exponential factor of the forward (ν_{for}) reaction step

[b] pre-exponential factor of the reverse (ν_{rev}) reaction step

[c] P_{N2O}=3.03E4 Pa; [d] P_{CH4}=1.52E4 Pa, being of 30 and 15 vol% under atmospheric pressure

Table S6. Elementary steps and kinetic parameters involved in microkinetic modeling over Cu dimer site of Cu-FER during N_2O-DMTM

Step	Elementary Steps	Reaction rate equations	${}^{a}v_{\mathrm{for}}$ (s^{-1})	${}^{b}v_{rev}{}^{-1}$ (s^{-1})	ΔE (eV)	ΔE^{-1} (eV)
R1	$\text{Z-Cu}_2 + \text{N}_2\text{O(g)} \leftrightarrow \text{Z-Cu}_2\text{-N}_2\text{O}$	$r_1 = k_1{}^{c}P_{\mathrm{N_2O}}\theta_{\mathrm{v}} - k_{-1}\theta_{\mathrm{N_2O}}$	0.02	2.09E10	-	0.95
R2	$\text{Z-Cu}_2\text{-N}_2\text{O} \leftrightarrow \text{Z-Cu}_2\text{-O} + \text{N}_2\text{(g)}$	$r_2 = k_2\theta_{\mathrm{N_2O}}$	4.01E13	-	0.89	-
R3	$\text{Z-Cu}_2\text{-O+CH}_4\text{(g)} \leftrightarrow \text{Z-Cu}_2\text{-CH}_3\text{-OH}$	$r_3 = k_3{}^{d}P_{\mathrm{CH_4}}\theta_{\mathrm{O}} - k_{-3}\theta_{\mathrm{CH_3-OH}}$	3.78E11	2.0E14	0.49	0.65
R4	$\text{Z-Cu}_2\text{-CH}_3\text{-OH} \leftrightarrow \text{Z-Cu}_2\text{-CH}_3\text{OH}$	$r_4 = k_4\theta_{\mathrm{CH_3\text{-}OH}} - k_{-4}\theta_{\mathrm{CH_3OH}}$	5.15E12	1.40E13	0.64	0.87
R5	$\text{Z-Cu}_2\text{-CH}_3\text{OH} \rightarrow \text{Z-Cu}_2 + \text{CH}_3\text{OH(g)}$	$r_5 = k_5\theta_{\mathrm{CH_3OH}}$	2.11E10	-	1.58	-

[a] pre-exponential factor of the forward (v_{for}) reaction step

[b] pre-exponential factor of the reverse (v_{rev}) reaction step

[c] P_{N2O}=3.03E4 Pa; [d] P_{CH4}=1.52E4 Pa, being of 30 and 15 vol% under atmospheric pressure

Table S7. Elementary steps and kinetic parameters involved in microkinetic modeling over dual Cu SA site of Cu-FER during N_2O-DMTM

Step	Elementary Steps	Reaction rate equations	[a]ν_{for} (s^{-1})	[b]ν_{rev}^{-1} (s^{-1})	ΔE (eV)	ΔE^{-1} (eV)
R1	$\text{Z-Cu}_{\text{Dual-SA}} + N_2O(g) \leftrightarrow \text{Z-Cu}_{\text{Dual-SA}}\text{-}N_2O$	$r_1 = k_1{}^{c}P_{N_2O}\theta_v - k_{-1}\theta_{N_2O}$	0.02	2.15E10	-	0.58
R2	$\text{Z-Cu}_{\text{Dual-SA}}\text{-}N_2O \leftrightarrow \text{Z-Cu-O} + N_2(g)$	$r_2 = k_2\theta_{N_2O}$	8.43E10	-	0.26	-
R3	$\text{Z-Cu-O+}CH_4(g) \leftrightarrow \text{Z-Cu} + CH_3OH(g)$	$r_3 = k_3{}^{d}P_{CH_4}\theta_O - k_{-3}{}^{e}P_{CH_3OH}\theta_v$	2.19E10	3.22E10	0.33	0.31

[a] pre-exponential factor of the forward (ν_{for}) reaction step

[b] pre-exponential factor of the reverse (ν_{rev}) reaction step

[c] P_{N2O}=3.03E4 Pa; [d] P_{CH4}=1.52E4 Pa, being of 30 and 15 vol% under atmospheric pressure

[e] P_{CH3OH}=555.3 Pa; being of equilibrium content during N_2O-DMEM over Cu-FER-0.3%

Table S8. Elementary steps and kinetic parameters involved in microkinetic modeling over Cu dimer site of Cu-FER during N_2O-DMTM to produce DME

Step	Elementary Steps	Reaction rate equations	$^{a}v_{\mathrm{for}}$ (s^{-1})	$^{b}v_{rev}^{-1}$ (s^{-1})	ΔE (eV)	ΔE^{-1} (eV)
R1	$\text{Z-Cu}_2 + \text{N}_2\text{O(g)} \leftrightarrow \text{Z-Cu}_2\text{-N}_2\text{O}$	$r_1 = k_1{}^{\mathrm{c}}P_{\mathrm{N_2O}}\theta_{\mathrm{v}} - k_{-1}\theta_{\mathrm{N_2O}}$	0.02	2.09E10	-	0.95
R2	$\text{Z-Cu}_2\text{-N}_2\text{O} \leftrightarrow \text{Z-Cu}_2\text{-O} + \text{N}_2\text{(g)}$	$r_2 = k_2\theta_{\mathrm{N_2O}}$	4.01E13	-	0.89	-
R3	$\text{Z-Cu}_2\text{-O+CH}_4\text{(g)} \leftrightarrow \text{Z-Cu}_2\text{-CH}_3\text{-OH}$	$r_3 = k_3{}^{\mathrm{d}}P_{\mathrm{CH_4}}\theta_{\mathrm{O}} - k_{-3}\theta_{\mathrm{CH_3-OH}}$	3.78E11	2.0E14	0.49	0.65
R4	$\text{Z-Cu}_2\text{-CH}_3\text{-OH} \leftrightarrow \text{Z-Cu}_2\text{-CH}_3\text{OH}$	$r_4 = k_4\theta_{\mathrm{CH_3\text{-}OH}} - k_{-4}\theta_{\mathrm{CH_3OH}}$	5.15E12	1.40E13	0.64	0.87
R5	$\text{Z-Cu}_2\text{-CH}_3\text{OH} \rightarrow \text{Z-Cu}_2 + \text{CH}_3\text{OH(g)}$	$r_5 = k_5\theta_{\mathrm{CH_3OH}}$	2.11E10	-	1.58	-
R6	$\text{Z-Cu-CH}_3\text{-OH+CH}_3\text{OH(g)} \rightarrow$ $\text{Z-Cu+DME(g)} + \text{H}_2\text{O(g)}$	$\mathrm{r}_6 = k_6\theta_{\mathrm{CH_3\text{-}OH}}{}^{\mathrm{d}}P_{\mathrm{CH_3OH}}$	5.63E+10	-	0.69	-

[a] pre-exponential factor of the forward (v_{for}) reaction step

[b] pre-exponential factor of the reverse (v_{rev}) reaction step

[c] P_{N2O}=3.03E4 Pa; [d] P_{CH4}=1.52E4 Pa, being of 30 and 15 vol% under atmospheric pressure

[d] P_{CH3OH}=555.3 Pa; being of equilibrium content during N_2O-DMEM over Cu-FER-0.3%

Table S9. Elementary steps and kinetic parameters involved in microkinetic modeling over monomeric $[Cu]^+$ site of Cu-FER during N_2O-DMTM to produce DME

Step	Elementary Steps	Reaction rate equations	${}^{a}v_{for}$ (s^{-1})	${}^{b}v_{rev}{}^{-1}$ (s^{-1})	ΔE (eV)	ΔE^{-1} (eV)
R1	$\text{Z-Cu} + N_2O(g) \leftrightarrow \text{Z-Cu-}N_2O$	$r_1 = k_1{}^{c}P_{N_2O}\theta_v - k_{-1}\theta_{N_2O}$	0.02	2.09E10	-	0.33
R2	$\text{Z-Cu-}N_2O \leftrightarrow \text{Z-Cu-O} + N_2(g)$	$r_2 = k_2\theta_{N_2O}$	1.78E13	-	1.35	-
R3	$\text{Z-Cu-O+}CH_4(g) \leftrightarrow \text{Z-Cu-}CH_3\text{-OH}$	$r_3 = k_3{}^{d}P_{CH_4}\theta_O - k_{-3}\theta_{CH_3-OH}$	3.18E12	2.81E14	0.12	1.71
R4	$\text{Z-Cu-}CH_3\text{-OH} \leftrightarrow \text{Z-Cu-}CH_3OH$	$r_4 = k_4\theta_{CH_3\text{-OH}} - k_{-4}\theta_{CH_3OH}$	6.58E12	2.49E13	0.42	1.27
R5	$\text{Z-Cu-}CH_3OH \rightarrow \text{Z-Cu} + CH_3OH(g)$	$r_5 = k_5\theta_{CH_3OH}$	2.11E10	1.12	-	-
R6	$\text{Z-Cu-}CH_3\text{-OH+}CH_3OH(g) \rightarrow$ $\text{Z-Cu+DME}(g) + H_2O(g)$	$r_6 = k_6\theta_{CH_3\text{-OH}}{}^{d}P_{CH_3OH}$	5.66E11	-	0.02	-

[a] pre-exponential factor of the forward (v_{for}) reaction step

[b] pre-exponential factor of the reverse (v_{rev}) reaction step

[c] P_{N2O}=3.03E4 Pa; [d] P_{CH4}=1.52E4 Pa, being of 30 and 15 vol% under atmospheric pressure

[d] P_{CH3OH}=555.3 Pa; being of equilibrium content during N_2O-DMEM over Cu-FER-0.3%

Table S10. Selected O-Al distances and calculated potential energy of mean force (PMF) during the constrained MD simulations for CH_3OH diffusion from 8MR into 10 MR of Cu-FER.

$d_{\text{O-Al}}$ (Å)	PMF (eV)
2.12	0.00
2.89	0.28
3.41	0.26
4.06	0.18
4.52	0.04
5.23	-0.22
6.31	-0.36

Table S11. Framework Al distribution over Cu-FER-0.3% base on deconvolution of ^{27}Al NMR spectrum

Cu-FER-0.3%	Chemical shift (ppm)	FWHM (ppm)	Peak area (a.u.)	Occupation ratio (%)
T1	61.3	0.58	15.4	0.5
T2	51.5	6.74	450.1	14.1
T3	53.3	4.54	1430.9	44.6
T4	55.2	3.28	1308.8	40.8

Table S12 Physicochemical properties of Cu-FER samples

Samples	[a]Cu loading (wt%)	[b]Crystal size (nm)	[c]Specific surface area (m^2/g)	[d]Micro pore volume (cm^3/g)
H-FER	0	41.5	378.6	0.34
Cu-FER-0.11%	0.11	42.6	391.4	0.34
Cu-FER-0.3%	0.30	37.5	372.4	0.34
Cu-FER-0.6%	0.6	38.6	359.5	0.33
Cu-FER-1%	1.0	40.0	386.7	0.33

[a] determined by ICP

[b] derived by Scherrer equation

[c] determined by N_2 adsorption/desorption

[d] determined by t-plot method

Table S13 Fe Impurity content detected by ICP-OES over Cu-FER samples

Samples	Fe content /ppm
H-FER	90
Cu-FER-0.11%	85
Cu-FER-0.3%	80
Cu-FER-0.6%	84
Cu-FER-1.0%	82

Table S14. Cu^+ quantitation by EPR over Cu-FER samples being respectively pretreated by He and N_2O.

Sample	**spins**	**m_{cat} (mg)**	**Counts/g**	**Cu dimer ratio**
Cu-FER-0.11%-N_2O	4.796e+16	4.0 mg	1.20E+19	18.5%
Cu-FER-0.11%-He	6.040e+16	3.9 mg	1.47E+19	
Cu-FER-0.3%-N_2O	5.05E+16	4.0	1.26E+19	20.0%
Cu-FER-0.3%-He	6.16E+16	3.9	1.58E+19	
Cu-FER-0.6%-N_2O	5.180e+16	3.8 mg	1.35E+19	25.4%
Cu-FER-0.6%-He	6.935e+16	3.9mg	1.81E+19	

Identification Category of Dual Cu SA

Dual Cu SA as Major Active Site for N_2O-DMTM over Cu-FER: In our study, we identified three types of active sites on Cu-FER namely monomeric $[Cu]^+$ cation site, dual Cu single atom site (dual Cu SA) and Cu dimer $[Cu\text{-}O\text{-}Cu]^{2+}$ site. The dual Cu SA site functions as the most active site for the N_2O-DMTM to generate CH_3OH, relative to others counterparts. Although the Cu dimer site play a significant role in the subsequent tandem catalytic reaction of ($CH_3OH \rightarrow$DME), the related reaction rate would be strongly determined by the initial CH_3OH production step to supply enough reactant of CH_3OH. Thereby, the dual Cu SA was proposed to be the major active site during N_2O-DMTM over Cu-FER.

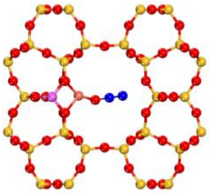	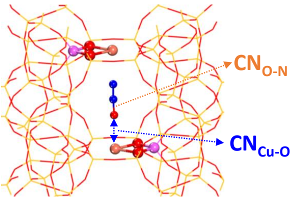	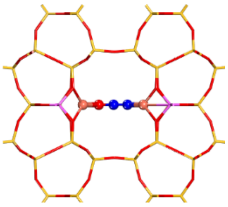
Monomeric [Cu]+	Dual Cu SA	Cu dimer
Cu monomer		$[Cu\text{-}O\text{-}Cu]^{2+}$

Illustration of Cu monomer and Cu dimer site

Dual Cu SA Site Belonging to Cu Monomer: Strictly speaking, such highly active dual Cu SA site belongs to the category of Cu monomer. Firstly, it is generated by two neighboring monomeric $[Cu]^+$ that is typically located at parallel 6 membered ring (MR) of 8 MR channel of FER (see diagram above). Secondly, after the interaction with N_2O, two neighboring Cu monomeric sites of $[Cu\text{-}O]^+$--$[Cu]^+$ would be generated. As noted, one Cu monomer of $[Cu\text{-}O]^+$ would be generated for the scenario of monomeric $[Cu]^+$ site. However, being entirely different, the $[Cu\text{-}O\text{-}Cu]^{2+}$ site would be generated cover the Cu dimer site which displays sluggish activity for the subsequent CH_4 activation than the monomeric $[Cu\text{-}O]^+$ site.

Reference

1. G. Zhao, E. Benhelal, A. Adesina, E. Kennedy and M. Stockenhuber, Comparison of Direct, Selective oxidation of methane by N_2O over Fe-ZSM-5, Fe-Beta, and Fe-FER catalysts, *J. Phys. Chem. C*, 2019, **123**, 27436-27447.
2. K. T. Dinh, M. M. Sullivan, K. Narsimhan, P. Serna, R. J. Meyer, M. Dincă and Y. Román-Leshkov, Continuous partial oxidation of methane to methanol catalyzed by diffusion-paired copper dimers in copper-exchanged zeolites, *J. Am. Chem. Soc.*, 2019, **141**, 11641-11650.
3. V. L. Sushkevich, D. Palagin, M. Ranocchiari and J. A. van Bokhoven, Selective anaerobic oxidation of methane enables direct synthesis of methanol, *Science*, 2017, **356**, 523-527.
4. R. Xu, N. Liu, C. Dai, Y. Li, J. Zhang, B. Wu, G. Yu and B. Chen, H_2O-built proton transfer bridge enhances continuous methane oxidation to methanol over Cu-BEA Zeolite, *Angew. Chem. Int. Ed.*, 2021, **60**, 16634-16640.
5. L. Xu, D. Mei and G. Henkelman, Adaptive kinetic Monte Carlo simulation of methanol decomposition on Cu(100), *J. Chem. Phys.*, 2009, **131**, 244520.
6. Q. Jin, B. Chen, Z. Ren, X. Liang, N. Liu and D. Mei, A theoretical study on reaction mechanisms and kinetics of thiophene hydrodesulfurization over MoS_2 catalysts, *Catal. Today*, 2018, **312**, 158-167.
7. Q.-X. Cai, J.-G. Wang, Y.-G. Wang and D. Mei, Mechanistic insights into the structure-dependent selectivity of catalytic furfural conversion on platinum catalysts, 2015, **61**, 3812-3824.
8. C. Dai, Y. Zhang, N. Liu, G. Yu, N. Wang, R. Xu and B. Chen, Mechanistic insight into the effect of active site motif structures on direct oxidation of methane to methanol over Cu-ZSM-5, *Phys. Chem. Chem. Phys.*, 2023, **25**, 24894-24903.
9. R. Xu, Z. Wang, N. Liu, C. Dai, J. Zhang and B. Chen, Understanding Zn functions on hydrothermal stability in a one-pot-synthesized Cu&Zn-SSZ-13 catalyst for NH_3 selective catalytic reduction, *ACS Catal.*, 2020, **10**, 6197-6212.
10. N. Liu, R. Zhang, B. Chen, Y. Li and Y. Li, Comparative study on the direct decomposition of nitrous oxide over M (Fe, Co, Cu)–BEA zeolites, *J. Catal.*, 2012, **294**, 99-112.
11. L. Sun, Y. Wang, C. Wang, Z. Xie, N. Guan and L. Li, Water-involved methane-selective catalytic oxidation by dioxygen over copper zeolites, *Chem*, 2021, **7**, 1557-1568.
12. K. T. Dinh, M. M. Sullivan, K. Narsimhan, P. Serna, R. J. Meyer, M. Dinca and Y. Roman-Leshkov, continuous partial oxidation of methane to methanol catalyzed by diffusion-paired copper dimers in copper-exchanged zeolites, *J. Am. Chem. Soc.*, 2019, **141**, 11641-11650.
13. Y. Deng, H. Lei, U. Simon, D. Ye and P. Chen, Transition-metal-promoted Cu-SSZ-13 catalysts for continuous selective oxidation of methane to methanol using molecular oxygen, *ACS Catal.*, 2023, **14**, 292-298.
14. B. Rungtaweevoranit, A. M. Abdel-Mageed, P. Khemthong, S. Eaimsumang, K. Chakarawet, T. Butburee, B. Kunkel, S. Wohlrab, K. Chainok, J. Phanthasri, S. Wannapaiboon, S. Youngjan, T. Seehamongkol, S. Impeng and K. Faungnawakij, Structural evolution of iron-loaded metal-organic framework catalysts for continuous gas-phase oxidation of methane to methanol, *ACS Appl. Mater. Interfaces*, 2023, **15**, 26700-26709.
15. J. Pokhrel and D. F. Shantz, Continuous partial oxidation of methane to methanol over Cu-SSZ-39 catalysts, *J. Catal.*, 2023, **421**, 300-308.
16. H. Zhang, J. Guo and Y. Cao, Continuous selective conversion of methane to methanol over a Cu-KFI zeolite catalyst using a water-O(2) mixture as the oxygen source, *Chem. Commun.*, 2023, **60**, 228-231.
17. A. Koishybay and D. F. Shantz, Water is the oxygen source for methanol produced in partial oxidation of methane in a flow reactor over Cu-SSZ-13, *J. Am. Chem. Soc.*, 2020, **142**, 11962-11966.

18. H. Zhang, X. Zhang, X. Shi, X. Liu, J. Liang, S. Li, S. Ma, X. Xiao, J. Guo, L. Zhang and M. Tan, Single-step conversion of methane-steam to methanol on single-atom Cu1/γ-Al_2O_3 catalyst prepared via electrostatic anchoring, *Appl. Catal. B*, 2025, **361**.
19. Y. R. Jeong, H. Jung, J. Kang, J. W. Han and E. D. Park, Continuous synthesis of methanol from methane and steam over copper-mordenite, *ACS Catal.*, 2021, **11**, 1065-1070.
20. C. Zhou, S. Li, S. He, Z. Zhao, Y. Jiao and H. Zhang, Temperature-dependant active sites for methane continuous conversion to methanol over Cu-zeolite catalysts using water as the oxidant, *Fuel*, 2022, **329**.
21. H. Zhang, P. Han, D. Wu, C. Du, J. Zhao, K. H. L. Zhang, J. Lin, S. Wan, J. Huang, S. Wang, H. Xiong and Y. Wang, Confined Cu-OH single sites in SSZ-13 zeolite for the direct oxidation of methane to methanol, *Nat. Commun.*, 2023, **14**, 7705.
22. A. V. Jagtap, P. Kumar, S. Gupta, A. Nagendra, S. N. Jha, D. Bhattacharyya, T. G. Ajithkumar and C. P. Vinod, Atmospheric-pressure continuous-flow methane oxidation to methanol and acetic acid using H_2O_2 over the Au–Fe catalyst, *ACS Sus. Chem. Eng.*, 2024, **12**, 8958-8967.
23. B. Ipek and R. F. Lobo, Catalytic conversion of methane to methanol on Cu-SSZ-13 using N_2O as oxidant, *Chem. Commun.*, 2016, **52**, 13401-13404.
24. O. Memioglu and B. Ipek, A potential catalyst for continuous methane partial oxidation to methanol using N_2O: Cu-SSZ-39, *Chem. Commun.*, 2021, **57**, 1364-1367.
25. I. Gokce, M. O. Ozbek and B. Ipek, Conditions for higher methanol selectivity for partial CH_4 oxidation over Fe-MOR using N_2O as the oxidant and comparison to Fe-SSZ-13, Fe-SSZ-39, Fe-FER, and Fe-ZSM-5, *J. Catal.*, 2023, **427**, 115113.
26. P. Xiao, Y. Wang, Y. Lu, T. De Baerdemaeker, A.-N. Parvulescu, U. Müller, D. De Vos, X. Meng, F.-S. Xiao, W. Zhang, B. Marler, U. Kolb, H. Gies and T. Yokoi, Effects of Al distribution in the Cu-exchanged AEI zeolites on the reaction performance of continuous direct conversion of methane to methanol, *Appl. Catal. B*, 2023, **325,** 122395.
27. P. Xiao, Y. Wang, K. Nakamura, Y. Lu, T. De Baerdemaeker, A.-N. Parvulescu, U. Müller, D. De Vos, X. Meng, F.-S. Xiao, W. Zhang, B. Marler, U. Kolb, R. Osuga, M. Nishibori, H. Gies and T. Yokoi, Highly Effective Cu/AEI zeolite catalysts contribute to continuous conversion of methane to methanol, *ACS Catal.* 2023, **13**, 11057-11068.